Thermodynamically stabilized β-$CsPbI_3$-based perovskite solar cells with efficiencies >18%

Yong Wang[1], M. Ibrahim Dar[2*], Luis K. Ono[3], Taiyang Zhang[1], Miao Kan[1], Yawen Li[4], Lijun Zhang[4], Xingtao Wang[1], Yingguo Yang[5], Xingyu Gao[5], Yabing Qi[3*], Michael Grätzel[2*] and Yixin Zhao[1,6*]

Affiliations:

[1]School of Environmental Science and Engineering, Shanghai Jiao Tong University, 800 Dongchuan Road, Shanghai 200240 (China).

[2]Laboratory of Photonics and Interfaces, Institute of Chemical Sciences and Engineering, Ecole Polytechnique Federale de Lausanne, CH-1015 Lausanne, Switzerland.

[3]Energy Materials and Surface Sciences Unit (EMSSU), Okinawa Institute of Science and Technology Graduate University (OIST), Okinawa 904-0495, Japan

[4] State Key Laboratory of Superhard Materials, Key Laboratory of Automobile Materials of MOE, and School of Materials Science and Engineering, Jilin University, Changchun 130012, China

[5] Shanghai Synchrotron Radiation Facility (SSRF), Zhangjiang Lab, Shanghai Advanced Research Institute, Chinese Academy of Sciences, 239 Zhangheng Road, Shanghai 201204, P. R. China.

[6] Shanghai Institute of Pollution Control and Ecological Security, Shanghai 200092, P.R. China

*Corresponding author. E-mail: yixin.zhao@sjtu.edu.cn (Y. Z.); michael.graetzel@epfl.ch (M.G.); Yabing.Qi@OIST.jp (Y. B. Q.); ibrahim.dar@epfl.ch (M. I. D.)

Abstract

Although β-$CsPbI_3$ has a band gap favorable for application in tandem solar cells, depositing and stabilizing β-$CsPbI_3$ experimentally has remained a challenge. We obtained highly crystalline β-$CsPbI_3$ films with an extended spectral response and enhanced phase stability. Synchrotron-based x-ray scattering revealed the presence of highly oriented β-$CsPbI_3$ grains, and sensitive elemental analyses including inductively coupled plasma mass spectrometry and time-of-flight secondary ion mass spectrometry confirmed their all-inorganic composition. We further mitigated the effects of cracks and pinholes in the perovskite layer by surface treating with choline iodide, which increased the charge carrier lifetime and improved the energy level alignment between the β-$CsPbI_3$ absorber layer and carrier selective contacts. The perovskite solar cells made from the treated material had highly reproducible and stable efficiencies reaching 18.4% under 45±5 Celsius ambient conditions.

One Sentence Summary: Highly Efficient and Thermodynamically Stable All-inorganic Cesium Lead Iodide Perovskite with Extended Spectral Response

The state-of-the-art power-conversation efficiencies (PCEs) reported for inorganic perovskite solar cells (PSCs), typically ~15%, are substantially lower than those of the hybrid organic-inorganic metal halide PSCs (as high as 24.2%), primarily because all-inorganic perovskites have larger band gaps and less favorable photophysical properties(*1-3*). Cesium lead iodide ($CsPbI_3$) has the most promising band gap for applications as two-level tandem solar cells in combination with silicon (*4, 5*), but the small size of Cs^+ gives rise to the unideal tolerance factor that makes it difficult to stabilize the $CsPbI_3$ perovskite phase under ambient conditions (*6-9*). Theoretical calculations predict that the tetragonal (β-phase) polymorph of $CsPbI_3$ can be crystallized at lower temperatures and would have a more stable perovskite structure than the cubic α-phase (*10-13*), but experimentally it has been challenging to deposit and stabilize β-$CsPbI_3$ for high-efficiency PSCs (*14*).

We have grown highly-stable β-$CsPbI_3$ perovskite films with extended ultraviolet-visible (UV-vis) absorbance and fabricated PSCs with 15.1% PCE. Furthermore, we developed a crack-filling interface engineering method using choline iodine (CHI), which not only passivated the surface trap states of perovskite but also led to better matching of the energy levels at the interfaces between the β-$CsPbI_3$ perovskite and the TiO_2 electron-transporting layer (ETL), as well as with the spiro-MeOTAD（2,2′,7,7′-tetrakis(N,N-bis(p-methoxyphenyl)amino)-9,9′-spirobifluorene) hole transport layer (HTL). With this approach, the efficiency of β-$CsPbI_3$ based PSCs was improved to 18.4% with high stability and reproducibility.

To mitigate the challenge of obtaining $CsPbI_3$ perovskite phase through conventional solvent engineering method involving PbI_2 and CsI precursors (Fig. S1), we spin-coated a precursor solution containing a stoichiometric mixture of $PbI_2 \cdot x$DMAI (x=1.1~1.2) and CsI onto a compact TiO_2 layer (Fig. S2-S5). After annealing at 210 °C for 5 min, the $CsPbI_3$ films showed an

absorbance edge ~736 nm (Fig. 1A) and a band gap of 1.68 eV as determined from a Tauc plot (Fig. S2), substantially redshifted relative to the ~1.73 eV value previously reported for $CsPbI_3$ films (*4*).

To rule out the incorporation of any organic A-site cations that could have caused this redshift, we used thermogravimetric analysis (TGA) and nuclear magnetic resonance (NMR) spectroscopy (Fig. S3-Fig. S4). Both techniques establish that an optimized annealing process of ~210 °C for 5 min was sufficient to remove all organic species. This conclusion was further supported by absorption and XRD data recorded for the samples annealed at ~210 °C for different periods of time (Fig. S5). We also evaluated the composition of the perovskite films by using inductively coupled plasma mass spectrometry (ICP-MS) and time-of-flight secondary ion mass spectrometry (TOF-SIMs) (Table S1 and Fig. S6). These methods confirmed that the perovskite films are all-inorganic. In contrast, ICP-MS and TOF-SIMs revealed a deficiency of Cs^+ and the presence of organic A-site cations (dimethylammonium) in perovskite films that were annealed at lower temperatures (100°C to 110°C) (*15*).

The desired redshift is associated with the phase of $CsPbI_3$ (*13*). To determine the crystal structure of the perovskite films, we used x-ray scattering (XRD) techniques, including synchrotron-based grazing incidence wide-angle x-ray scattering (GIWAXS). We indexed the XRD patterns to β-$CsPbI_3$ (Fig. 1B and Fig. S7), a phase of $CsPbI_3$ previously observed only above 230°C. Although the XRD pattern measured at room temperature will not be identical to the standard XRD pattern obtained at higher temperature due to the lattice thermal expansion, the basic features of the patterns should be very similar and the in-situ temperature dependent GWAXS pattern of our β-$CsPbI_3$ only show small variation between 30 to 250 °C (Fig. S8-S9). Relatively intense (110) and (220) reflections further indicate a preferred (110) orientation of the

β-$CsPbI_3$ grains. Powder samples obtained from scratching the $CsPbI_3$ films revealed peak splitting at 28° to 29° for 2θ (Fig. 1B), as expected for the tetragonal β-$CsPbI_3$ phase. The pattern was quite different from those of α- and γ-$CsPbI_3$ systems (Fig.S10). Notably, most of the previously reported XRD patterns that have been incorrectly indexed to the "α-$CsPbI_3$" phase that actually correspond to γ-$CsPbI_3$, in accordance with the large band gap of ~1.73 eV of the latter system.

The GIWAXS data (Fig.1C) not only established the formation of β-$CsPbI_3$, but also revealed peak splitting of the tetragonal crystallites in the (220) class of reflections. Radially integrated intensity plots (Fig. S11) along the ring at q=10 nm^{-1} (scattering vector, $q=4\pi\sin(\theta)/\lambda$) at azimuthal angles of 90° further indicate a strong preferred (110) orientation of the β-$CsPbI_3$ grains. First-principles modeling that used theoretically optimized structures (Fig. S12) rationalized the lower band gap of tetragonal β-$CsPbI_3$ relative to orthorhombic γ-$CsPbI_3$ in terms of the degree of distortion away from the ideal cubic structure.

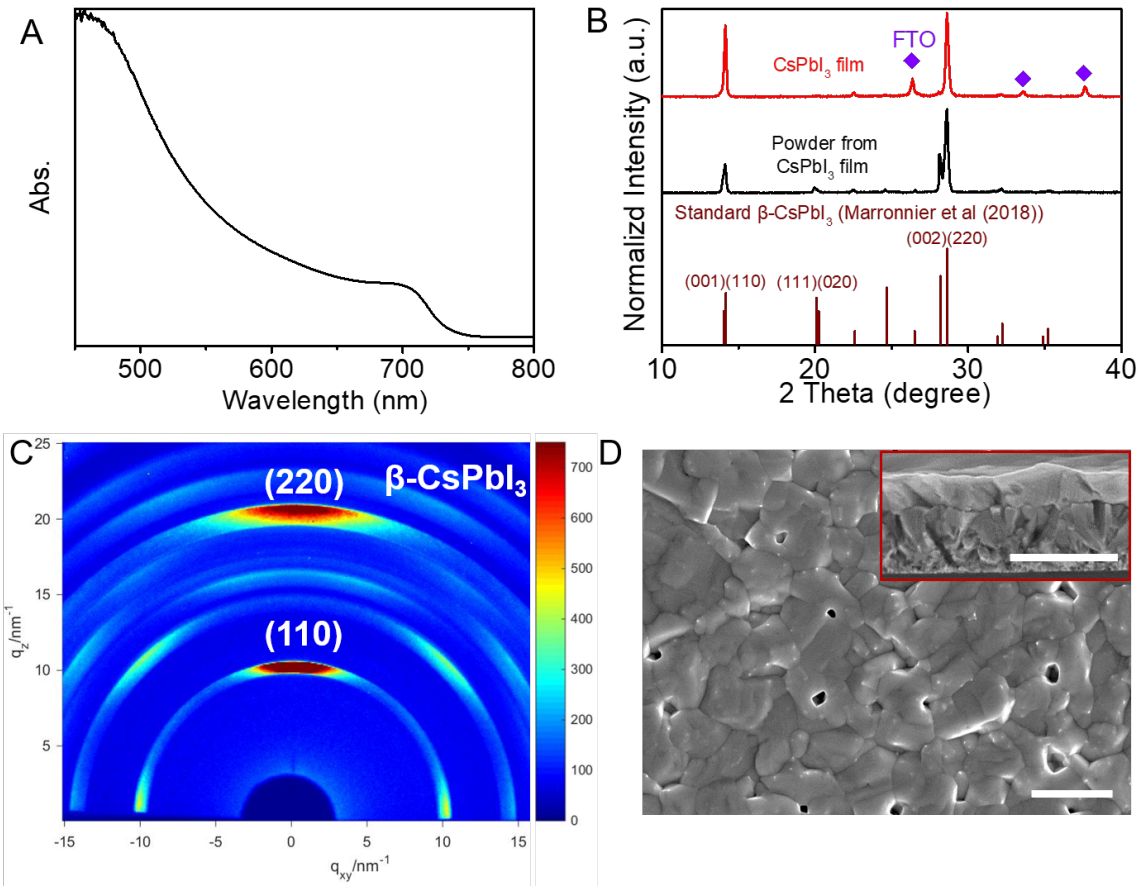

Fig. 1. Spectroscopic, structural and morphological characterization of β-$CsPbI_3$ thin film. (A) UV-vis spectrum. (B) XRD patterns acquired from a $CsPbI_3$ thin film and powders scratched from the films. Brown lines in Fig. 1B indicate the standard β-$CsPbI_3$ XRD pattern calculated for Cu Kα1 radiation for the tetragonal perovskite structure determined by Marronnier et al. at 518 K (*13*). (C) GIWAXS data from β-$CsPbI_3$ films. (D) Top-surface SEM image of β-$CsPbI_3$, the inset image in (D) presents the cross-sectional morphology of the β-$CsPbI_3$ perovskite thin film, scale bars represent 1 μm.

Scanning electron microscopy (SEM) revealed that the 350 to 400 nm thick β-$CsPbI_3$ perovskite films were composed of submicrometer-sized grains (Fig. 1D) comparable to the film thickness, and enables efficient charge extraction (*16*). Previous studies on $CsPbI_3$ reported that smaller grain size can improve perovskite phase stability and also suggested poor stability of β-$CsPbI_3$

phase at low temperature, so we further evaluated the thermal stability of highly crystalline β-$CsPbI_3$ (*7, 14*). The β-$CsPbI_3$ films, without any additional treatment, retained their color and phase even after annealing at 70 °C for >200 h in the nitrogen glovebox (Fig. S13). Compared to $MAPbI_3$, the β-$CsPbI_3$ films also exhibited better phase stability (Fig. S14). However, they turned into the undesired yellow phase when exposed to 85±5% relative humidity (RH) at 30°C after several minutes (Fig. S15).

We fabricated planar PSCs with the configuration of FTO/c-TiO_2/perovskite/spiro-OMeTAD/Ag, where FTO is fluorine-doped tin oxide and c-TiO_2 is compact TiO_2. Under standard 1.5G illumination, the best β-$CsPbI_3$ PSC showed a PCE of 15.1% with a short-circuit photocurrent density (J_{sc}) =20.03 mA·cm^{-2}, an open circuit photovoltage (V_{oc}) =1.05 V, and a fill factor (*FF*)=0.72 (Fig. S16). This state-of-the-art efficiency for an all-inorganic perovskite is still substantially lower than the PCEs reported for the PSCs based on organic-inorganic hybrid perovskites with band gap near that of β-$CsPbI_3$. The large hysteresis presents an additional caveat. The low efficiency of β-$CsPbI_3$ PSCs is mainly related to the modest V_{oc} and *FF* (Fig. S16). Previous studies have suggested that the reduced V_{oc} and *FF* could be associated with the poor band alignment and nonradiative carrier recombination at the surface defects (*17-19*).

To further improve the PCE of β-$CsPbI_3$ PSCs, we used the cracks present on the perovskite films to passivate the grains and simultaneously improve the alignment between perovskite and ETL layer. We selected CHI, which has been previously used to passivate hybrid perovskite films (*20*). We spin-coated CHI from isopropanol (IPA) solution (1 mg·mL^{-1}) onto β-$CsPbI_3$ thin films, CHI- treated β-$CsPbI_3$ being labeled as CHI-$CsPbI_3$ (Fig. 2A). The SEM images (Fig. S17) and carbon distribution profiles across the perovskite layer (Fig. 2B-2C and Fig. S18) indicate that the CHI penetrates into the bulk of the $CsPbI_3$ thin films, possibly through the pinholes and

cracks. This CHI-treatment improved the energy-level alignment of conduction-band minimum (CBM) between the β-$CsPbI_3$ and the TiO_2 by 120 meV (Fig. 2D-2F and Fig. S19). Furthermore, the CHI-treatment led to better energy-level alignment at both the β-$CsPbI_3$/ETL interface and the β-$CsPbI_3$/HTL interface.

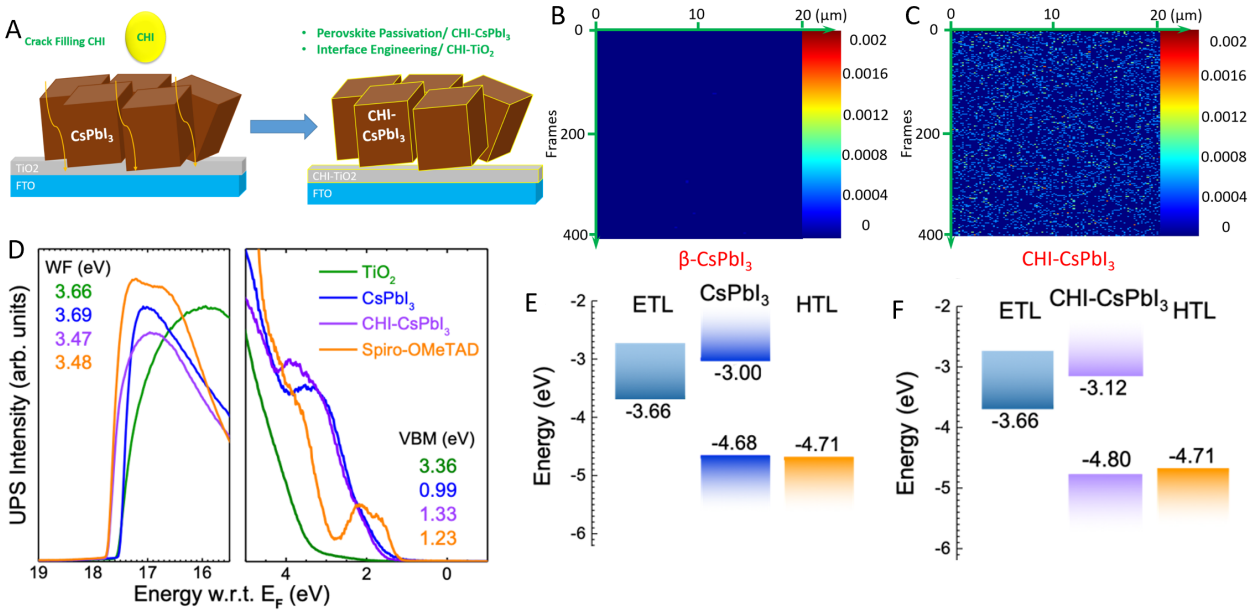

Fig. 2. Effect of crack filling interface engineering treatment on the energy level alignment. (A) Schematic illustration of crack-filling interface engineering. Comparison of cross-sectional carbon element analysis for the (B) β-$CsPbI_3$ and (C) CHI-$CsPbI_3$ films measured by TOF-SIMS. (D) UPS spectra (using the He-I line with photon energy of 21.22 eV) corresponding to the secondary electron onset region and valence band region of the as-prepared $CsPbI_3$, CHI-$CsPbI_3$ perovskite films, TiO_2 (ETL), and HOMO of the spiro-MeOTAD (HTL). (E) Corresponding energy diagram of the $CsPbI_3$ film and (F) CHI-$CsPbI_3$ film together with TiO_2 ETL and spiro-MeOTAD HTL that constitute the solar cell architecture.

The CHI-treatment had a negligible effect on the absorption features as the absorbance edge of CHI-$CsPbI_3$ films is still ~736 nm (~1.68 eV) (Fig. 3A). Likewise, the XRD patterns of pristine

and CHI-$CsPbI_3$ perovskite films (Fig. 1B and 3B) were almost identical. The comparison of Fig. 3C and S16 shows that the CHI homogeneously distributes on the surface of film and the pinhole locations are filled with CHI. The NMR based quantitative analysis revealed the CHI is only about 1%wt. of CHI-$CsPbI_3$ film (Fig. S20). The XRD patterns, UV-vis absorption spectra, and surface morphology of the β-$CsPbI_3$ perovskite thin films treated with the CHI solution with different concentrations are presented in Fig. S21.

The high-resolution cross-sectional SEM images (Fig. S22 A) revealed continuous monolithic type grains extending vertically across the entire $CsPbI_3$ film thickness but some pinholes in the bulk of the films. The subsequent CHI spin-coating treatment only filled these pinholes and cracks and did not lead to substantial disruptions in the structure, morphology and absorption properties of the β-$CsPbI_3$ films (Fig. S22 B). To exclude the effect of IPA solvent, the $CsPbI_3$ films treated only by IPA was further characterized by SEM (Fig. S23), which showed similar morphology with the $CsPbI_3$ films.

We also investigated the impact of CHI-treatment on the excitonic quality of perovskite films using time-resolved photoluminescence (TRPL) spectroscopy. The charge carriers are relatively long-lasting in case of CHI-$CsPbI_3$ films (Fig. 3D), which is likely the result of a reduction in nonradiative recombination by trap passivation, which improved the overall charge carrier dynamics. We calculated Urbach energies (Fig. S24)(*21, 22*) of 15.9 meV for $CsPbI_3$ and 14.4 meV for CHI-$CsPbI_3$. The Urbach energy for the CHI-$CsPbI_3$ should correspond to a lower density of trap states consisting well with the TRPL result.

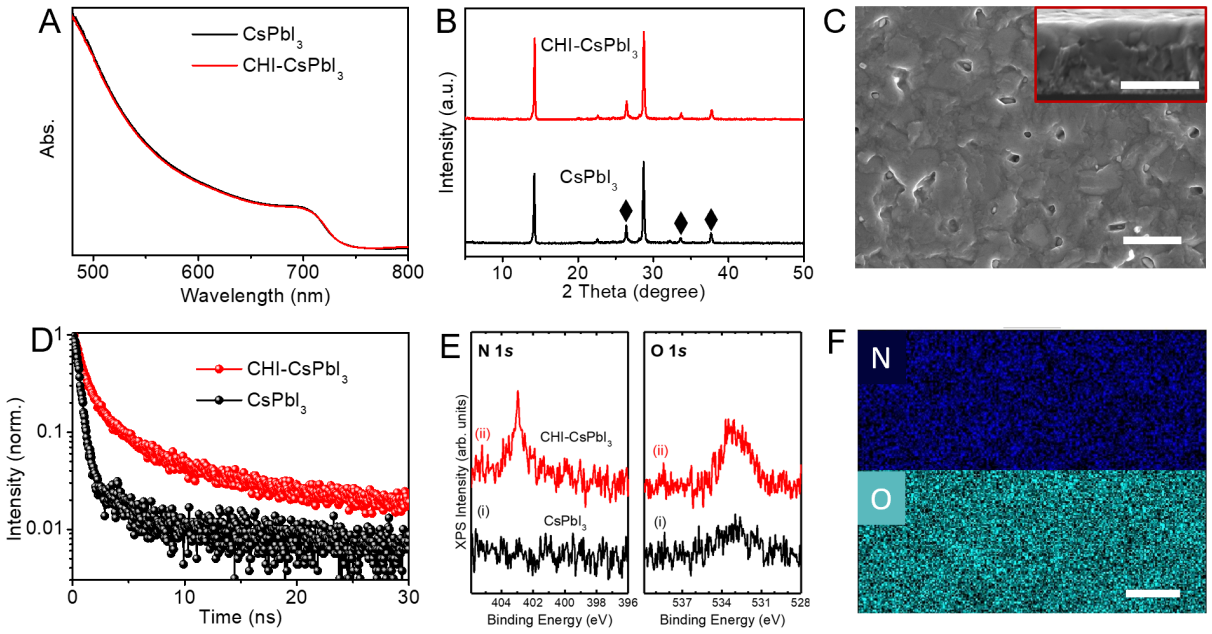

Fig. 3. Effects of CHI treatment on the spectroscopic and structural of β-$CsPbI_3$ perovskite thin films. (A) UV-vis spectra, (B) XRD patterns and (C) top-surface SEM image of CHI-$CsPbI_3$ perovskite thin films, diamond symbols correspond to FTO substrate. The inset image in (C) is the cross-section morphology of the CHI-$CsPbI_3$ perovskite thin films. (D) TRPL decay curves of $CsPbI_3$ and CHI-$CsPbI_3$ thin films. (E) XPS (Al-K = 1486.6 eV) N 1*s* and O 1*s* core-level spectra for the CHI-$CsPbI_3$ sample. EDX top view element mapping of (F) N and O elements distribution on the surface of CHI-$CsPbI_3$ perovskite thin films. The scale bar represents 1μm.

X-ray photoelectron spectroscopy (XPS) measurements were conducted to further explore the effect of CHI treatment on the chemical composition of perovskite films. All core-level peaks were assigned to Cs, Pb, I, C, N, and O (Fig. 3E and Fig. S25). The absence of (Ti 2*p*) peak confirmed the uniformity of coverage of the perovskite film on top of the TiO_2 substrate. No binding energy (BE) shifts or additional peaks were observed for Cs 3*d*, Pb 4*f*, I 3*d* establishing

that the CHI treatment improves the interfacial properties without changing the chemical nature of all-inorganic $CsPbI_3$ perovskite photoactive layer (Fig. S25). A small O 1*s* peak was also observed for the pristine β-$CsPbI_3$ sample (Fig. 3E), possibly a result of a small amount of oxygen adsorbed on the sample surface and/or diffused into the sample during the sample preparation in dry-O_2 conditions (*23*). Furthermore, energy-dispersive x-ray spectroscopy (EDX) elemental mapping (Fig. 3F and Fig. S26) shows a uniform distribution of N and O on the surface of CHI-$CsPbI_3$. More importantly, the CHI-$CsPbI_3$ perovskite thin films exhibited greater resistance toward humidity and also showed good thermal stability (Figs. S27-S28).

We compared the *J-V* characteristics of the best-performing PSCs based on CHI-$CsPbI_3$ and β-$CsPbI_3$ perovskite films (Fig. 4A). Although the *J*sc remained unaffected, the CHI-$CsPbI_3$-based PSC showed better V_{oc} (1.11 vs. 1.05 V) and *FF* (0.82 vs. 0.72) (Fig. 4B), improving the overall PCE from 15.1% to 18.4%, and we also obtained a certified PCE of 18.3% for CHI-$CsPbI_3$-based PSC (Fig. S29). We attributed this improvement to better energy level alignment and desired charge carrier dynamics. All *J-V* curves were measured at ~45±5 °C under full-sun illumination. Figure S30 shows that the efficiency drops marginally at ~ 60 °C. Furthermore, the CHI-$CsPbI_3$ based PSCs exhibit a smaller hysteresis, resulting in a stabilized output power of 17.8% (Fig. S31 and S32). The external quantum efficiency (EQE) of CHI-$CsPbI_3$ based PSC (Fig. 4C) > 90% for wavelengths between 500 and 600 nm. The integrated J_{SC} of 19.85 $mA \cdot cm^{-2}$ calculated from the EQE is comparable to the values (19.71 $mA \cdot cm^{-2}$) estimated for the pure $CsPbI_3$ device, corroborating with the JV characteristics. Furthermore, the PV performance of CHI treated $CsPbI_3$ using 0.5 mg/mL or 2 mg/mL also exhibited ~17% PCE, which was much higher than that of pure β-$CsPbI_3$ based devices (Fig. S33).

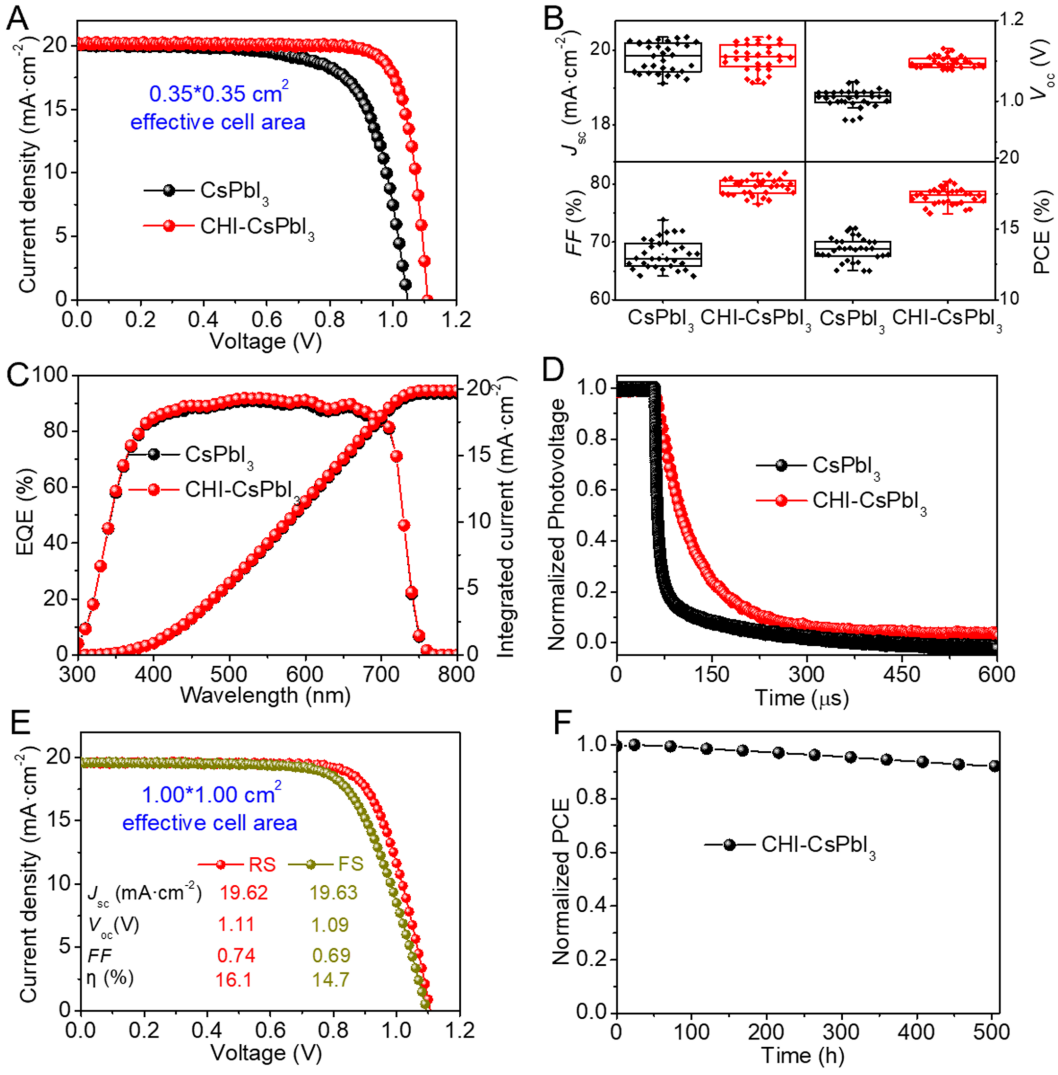

Fig. 4. Photovoltaic and device characterization. (A) J-V characteristics of PSCs based on $CsPbI_3$ and CHI-$CsPbI_3$ with 0.1 cm^2 effective cell area under simulated AM 1.5G solar illumination of 100 $mW \cdot cm^{-2}$ in reverse scan and (B) Corresponding PV metrics (0.1 cm^2 effective cell area; 32 devices). All *J-V* curves were measured at ~45±5 °C under full-sun illumination. (C) EQE spectrum together with the integrated J_{SC} for the $CsPbI_3$- and CHI-$CsPbI_3$ based PSCs. (D) TPV of $CsPbI_3$ and CHI-$CsPbI_3$ based PSCs. (E) J-V characteristics of PSCs based on CHI-$CsPbI_3$ with 1 cm^2 effective cell area under simulated AM 1.5G solar illumination of 100 $mW \cdot cm^{-2}$ in reverse scan. (F) Photostability of the un-encapsulated CHI-$CsPbI_3$ PSC

devices under continuous white light LED illumination (100mW·cm^{-2}) at their MPP in a N_2 glovebox.

We further investigated the CHI-treatment PSCs charge-transport properties with transient photocurrent decay (TPC) and photovoltage decay (TPV) measurements. Similar TPC responses (Fig. S34) suggest that the CHI treatment had minimal influence on the charge transport or charge collection efficiency, in agreement with J_{sc} and EQE results. In contrast, the TPV revealed that CHI-treatment increased charge-carrier lifetime (Fig. 4D) indicating a decrease in the undesired charge-carrier recombination(*24, 25*).

We fabricated large-area PSCs based on CHI-$CsPbI_3$ thin films. The champion CHI-$CsPbI_3$ devices, fabricated on 2.5-cm by 2.5-cm substrates with an effective cell area of 1 cm^2 (Fig. 4E), displayed a PCE of 16.1% with J_{SC} of 19.62 mA·cm^{-2}, V_{OC} of 1.11 V, and FF of 0.74 under reverse scan condition. The PV metrics (Fig. S35 and Table S2) showed an average efficiency as high as 15.2%. These large-area devices also showed small hysteresis (Fig. 4E), and high EQE and stabilized PCE (Figs. S36-37). Furthermore, the CHI-$CsPbI_3$ based PSCs stored in a N_2 glovebox retained 92% of their initial PCE after 500 h continuous illumination at maximum power point (MPP) (Fig. 4F). The CHI-$CsPbI_3$ based PSCs stored in a dark dry box (RH<10%) with oxygen shows no PV performance decay (Fig. S38 A). The encapsulated device shows excellent ambient stability (Fig. S38 B). The encapsulated device retained 95% of their initial PCE in air after 240 h continuous illumination and maximum power point tracking at MPP (Fig. S38 C and D).

Reference and notes

1. A. Swarnkar *et al.*, Quantum dot-induced phase stabilization of α-$CsPbI_3$ perovskite for high-

efficiency photovoltaics. *Science* **354**, 92-95 (2016).

2. P. Wang *et al.*, Solvent-controlled growth of inorganic perovskite films in dry environment for efficient and stable solar cells. *Nat. Commun.* **9**, 2225 (2018).
3. B. Zhao *et al.*, Thermodynamically Stable Orthorhombic γ-$CsPbI_3$ Thin Films for High-Performance Photovoltaics. *J. Am. Chem. Soc.* **140**, 11716-11725 (2018).
4. G. E. Eperon *et al.*, Inorganic caesium lead iodide perovskite solar cells. *J. Mater. Chem. A* **3**, 19688-19695 (2015).
5. E. M. Sanehira *et al.*, Enhanced mobility $CsPbI_3$ quantum dot arrays for record-efficiency, high-voltage photovoltaic cells. *Sci. Adv.* **3**, eaao4204 (2017).
6. S. Dastidar *et al.*, High Chloride Doping Levels Stabilize the Perovskite Phase of Cesium Lead Iodide. *Nano Lett.* **16**, 3563-3570 (2016).
7. T. Zhang *et al.*, Bication lead iodide 2D perovskite component to stabilize inorganic α-$CsPbI_3$ perovskite phase for high-efficiency solar cells. *Sci. Adv.* **3**, e1700841 (2017).
8. B. Li *et al.*, Surface passivation engineering strategy to fully-inorganic cubic $CsPbI_3$ perovskites for high-performance solar cells. *Nat. Commun.* **9**, 1076 (2018).
9. A. K. Jena, A. Kulkarni, Y. Sanehira, M. Ikegami, T. Miyasaka, Stabilization of α-CsPbI3 in Ambient Room Temperature Conditions by Incorporating Eu into $CsPbI_3$. *Chem. Mater.* **30**, 6668-6674 (2018).
10. R. J. Sutton *et al.*, Cubic or Orthorhombic? Revealing the Crystal Structure of Metastable Black-Phase $CsPbI_3$ by Theory and Experiment. *ACS Energy Lett.*, 1787-1794 (2018).
11. C. C. Stoumpos, M. G. Kanatzidis, The Renaissance of Halide Perovskites and Their Evolution as Emerging Semiconductors. *Acc. Chem. Res.* **48**, 2791-2802 (2015).
12. C. C. Stoumpos, C. D. Malliakas, M. G. Kanatzidis, Semiconducting tin and lead iodide

perovskites with organic cations: phase transitions, high mobilities, and near-infrared photoluminescent properties. *Inorg. Chem.* **52**, 9019-9038 (2013).

13. A. Marronnier *et al.*, Anharmonicity and Disorder in the Black Phases of Cesium Lead Iodide Used for Stable Inorganic Perovskite Solar Cells. *ACS Nano* **12**, 3477-3486 (2018).
14. Y. Fu *et al.*, Selective Stabilization and Photophysical Properties of Metastable Perovskite Polymorphs of $CsPbI_3$ in Thin Films. *Chem. Mater.* **29**, 8385-8394 (2017).
15. W. Ke, I. Spanopoulos, C. C. Stoumpos, M. G. Kanatzidis, Myths and reality of HPbI3 in halide perovskite solar cells. *Nat. Commun.* **9**, 4785 (2018).
16. N. J. Jeon *et al.*, A fluorene-terminated hole-transporting material for highly efficient and stable perovskite solar cells. *Nat. Energy* **3**, 682-689 (2018).
17. N. Arora *et al.*, High Open-Circuit Voltage: Fabrication of Formamidinium Lead Bromide Perovskite Solar Cells Using Fluorene–Dithiophene Derivatives as Hole-Transporting Materials. *ACS Energy Lett.* **1**, 107-112 (2016).
18. H. Chen *et al.*, Molecular Engineered Hole-Extraction Materials to Enable Dopant-Free, Efficient p-i-n Perovskite Solar Cells. *Adv. Energy Mater.* **7**, 1700012 (2017).
19. Y. Shao, Y. Yuan, J. Huang, Correlation of energy disorder and open-circuit voltage in hybrid perovskite solar cells. *Nat. Energy* **1**, 15001 (2016).
20. X. Zheng *et al.*, Defect passivation in hybrid perovskite solar cells using quaternary ammonium halide anions and cations. *Nat. Energy* **2**, 17102 (2017).
21. P. Loper *et al.*, Complex Refractive Index Spectra of $CH_3NH_3PbI_3$ Perovskite Thin Films Determined by Spectroscopic Ellipsometry and Spectrophotometry. *J. Phys. Chem. Lett.* **6**, 66-71 (2015).
22. W. Zhang *et al.*, Enhanced optoelectronic quality of perovskite thin films with

hypophosphorous acid for planar heterojunction solar cells. *Nat. Commun.* **6**, 10030 (2015).

23. L. K. Ono *et al.*, Air-Exposure-Induced Gas-Molecule Incorporation into Spiro-MeOTAD Films. *J. Phys. Chem. Lett.* **5**, 1374-1379 (2014).
24. H. Tan *et al.*, Efficient and stable solution-processed planar perovskite solar cells via contact passivation. *Science* **355**, 722-726 (2017).
25. T. Leijtens *et al.*, Carrier trapping and recombination: the role of defect physics in enhancing the open circuit voltage of metal halide perovskite solar cells. *Energy Environ. Sci.* **9**, 3472-3481 (2016).
26. G. Kresse, J. Furthmüller, Efficiency of ab-initio total energy calculations for metals and semiconductors using a plane-wave basis set. *Comp. Mater. Sci.* **6**, 15-50 (1996).
27. G. Kresse, J. Furthmüller, Efficient iterative schemes for ab initio total-energy calculations using a plane-wave basis set. *Phys. Rev. B* **54**, 11169-11186 (1996).
28. P. E. Blöchl, Projector augmented-wave method. *Phys. Rev. B* **50**, 17953-17979 (1994).
29. J. P. Perdew, K. Burke, M. Ernzerhof, Generalized Gradient Approximation Made Simple. *Phys. Rev. Lett.* **77**, 3865-3868 (1996).
30. A. V. Krukau, O. A. Vydrov, A. F. Izmaylov, G. E. Scuseria, Influence of the exchange screening parameter on the performance of screened hybrid functionals. *J. Chem. Phys.* **125**, 224106 (2006).
31. D. Cahen, A. Kahn, Electron Energetics at Surfaces and Interfaces: Concepts and Experiments. *Adv. Mater.* **15**, 271-277 (2003).
32. A. Kahn, Fermi level, work function and vacuum level. *Mater. Horiz.* **3**, 7-10 (2016).
33. L. Qiu *et al.*, Engineering Interface Structure to Improve Efficiency and Stability of Organometal Halide Perovskite Solar Cells. *J. Phys. Chem. B* **122**, 511-520 (2018).

34. D. Cahen, A. Kahn, E. Umbach, Energetics of molecular interfaces. *Mater. Today* **8**, 32-41 (2005).

35. Z. Wu *et al.*, Improved Efficiency and Stability of Perovskite Solar Cells Induced by CO Functionalized Hydrophobic Ammonium-Based Additives. *Adv. Mater.* **30**, 1703670 (2018).

ACKNOWLEDGMENTS

We thank Instrumental Analysis Center (School of Environmental Science and Engineering and Shanghai Jiao Tong University) providing the time and help on material characterization tests. We also thank the third certification institutions National Institute of Metrology (China) for authentication tests. **Funding:** This work performed at Shanghai Jiaotong University was supported by the NSFC (Grants Nos. 21777096, 51861145101), Huoyingdong Grant (151046), Shanghai Shuguang Grant (17SG11) and the China Postdoctoral Science Foundation (2017M621466). The work performed at the Okinawa Institute of Science and Technology Graduate University was supported by funding from the Energy Materials and Surface Sciences Unit of the Okinawa Institute of Science and Technology Graduate University, the OIST R&D Cluster Research Program, the OIST Proof of Concept (POC) Program, and JSPS KAKENHI Grant Number JP18K05266, the work performed at Jilin University was supported by the National Natural Science Foundation of China (Grant No. 61722403 and 11674121). M.I.D acknowledges the financial support from the Swiss National Science Foundation under the project number P300P2_174471. Dr.Yingguo Yang and Dr. Xingyu Gao acknowledge the support of the National Key Research and Development Program of China (2017YFA0403400).Calculations were performed at High Performance Computing Center of Jilin University; **Authors contributions:** Y. Z., Y. B. Q. and M. G. designed and directed the study. Y.W., T. Z. conceived and performed the device fabrication work. Y. L. and L. Z. performed on the first first-principles calculations and analyzed the results. Y.W., M. I. D., L. K.O., T. Z., M. K., X.W., Y.Y., X.G., Y. L., L. Z., Y.Q., M.G., Y.Z. were involved in characterization and data analysis. All authors contributed to the discussions. Y.W., Y. Z., M.I.D., Y. B. Q., M. G. wrote the manuscript from all authors' input. All authors reviewed the paper; **Competing interests:** None declared. **Data and materials availability:** The data that support the findings of this study are available from the corresponding author upon reasonable request. All (other) data needed to evaluate the conclusions in the paper are present in the paper or the Supplementary Materials.

Supplementary Materials:

Science AAAS

Accepted Manuscript

Supplementary Materials for

Thermodynamically stabilized β-$CsPbI_3$-based perovskite solar cells with efficiencies >18%

Yong Wang[1], M. Ibrahim Dar[2*], Luis K. Ono[3], Taiyang Zhang[1], Miao Kan[1], Yawen Li[4], Lijun Zhang[4], Xingtao Wang[1], Yingguo Yang[5], Xingyu Gao[5], Yabing Qi[3*], Michael Grätzel[2*] and Yixin Zhao[1,6*]

Correspondence to: yixin.zhao@sjtu.edu.cn (Y. Z.); michael.graetzel@epfl.ch (M.G.); Yabing.Qi@OIST.jp (Y. B. Q.); ibrahim.dar@epfl.ch(M. I. D.)

This PDF file includes:

Materials and Methods

Materials

The CsI, PbI_2, and Choline Iodine (CHI) were purchased from Alfa Aesar. Anhydrous dimethylformamide (DMF) and isopropanol (IPA) were purchased from Sigma-Aldrich. The $PbI_2 \cdot x$DMAI (x=1.1-1.2) was prepared by mixing PbI_2 and 57% w/w hydroiodic acid (molar ratio 1:1.2) in DMF with stirring for 6 h at 60 °C. The excess HI was used to ensure complete conversion of PbI_2 into $PbI_2 \cdot x$DMAI. The precipitates were recovered by evaporating the solutions at 80 °C under a very high vacuum condition. Finally, the resulting solid was centrifuged and washed with several times copious diethyl ether and ethyl alcohol to remove the residuary solvent, respectively. The collected powders are dried in a vacuum oven at 70 °C for 24 h. The concentration of PbI_2 in the final product should be within the range of 69 to 71 weight %.

Device Fabrication

The laser patterned FTO (TEC-7) substrate was coated with a compact TiO_2 layer by spray pyrolysis of 0.2 M Ti (IV) bis (ethyl acetoacetate)-diisopropoxide in 1-butanol solution at 450 °C, followed by annealing at 450 °C for 1 h. The 0.6 M $CsPbI_3$ perovskite precursor was prepared by dissolving stoichiometric CsI, $PbI_2 \cdot x$DMAI with 1:1 molar ratio in DMF. Then, the $CsPbI_3$ active layer was spin-coated on 70 °C pre-warmed c-TiO_2/FTO substrate (3000rpm, 30s) with 210 °C annealing treatment for 5 min in a dry box with a <10 % RH. The annealed perovskite films were post-treated with 100 μL x mg·mL^{-1} CHI (x=0.5, 1, 2, corresponding samples are labeled as 0.5 CHI-$CsPbI_3$, CHI-$CsPbI_3$, 2 CHI-$CsPbI_3$, respectively) isopropanol solution via spin-coating (3000rpm, 30s). Finally, the post-treated perovskite films were heated at 100 °C for 5 min.

A layer of hole transport material (HTM) was spin-coated on top of the annealed films, which consisted of 0.1 M spiro-MeOTAD, 0.035 M bis(trifluoromethane) sulfonamide lithium salt (Li-TFSi), and 0.12 M 4-tert-butylpyridine (tBP) in chlorobenzene/acetonitrile (10:1, v/v) solution at 4000 rpm for 25 s. Finally, a 100-nm thick Ag layer was deposited by thermal evaporation at a constant evaporation rate of 0.3 Å/s.

Characterizations

The electronic properties of $CsPbI_3$, CHI-$CsPbI_3$, ETL and HTL films were characterized by ultraviolet photoemission spectroscopy (UPS, Kratos AXIS ULTRA HAS, He−Iα = 21.22 eV). The analysis of UPS was complemented by X-ray photoelectron spectroscopy (XPS, Kratos AXIS ULTRA HAS, monochromated Al Kα = 1486.6 eV). XPS was performed to probe the chemical states of the as-prepared $CsPbI_3$ and CHI-$CsPbI_3$. The binding energy (BE) values for UPS and XPS were calibrated by measuring the Fermi edge (E_F = 0 eV) and Au $4f_{7/2}$ (84.0 eV) on a clean Au surface, respectively. The estimated energy resolutions of UPS and XPS are 0.14 and 0.7 eV, respectively. Analysis of the XPS data was performed using Casa XPS 2.3.16 software. Five consecutive spectra were taken to evaluate possible UV and X-ray induced sample damage. Comparison of these spectra confirms minimal sample damage for $CsPbI_3$ and CHI-$CsPbI_3$ samples. The time acquisition for each scan in UPS was 15 s. For XPS, the acquisition time varied from 60 to 100 s depending on the core level regions. The five scans were averaged to a single spectrum to improve the signal to noise ratio.

The crystal structures of the formed perovskite films were characterized using XRD (Shimadzu XRD-6100 diffractometer with Cu Kα radiation). The perovskite films were characterized using SEM with an EDX (JEOL JSM-7800F Prime). A Time-of-Flight Secondary-Ion Mass Spectrometry (TOF-SIMS) (GAIA3 GMU Model 2016/*GAIA3) was used to

elemental mapping the perovskite films. 1H-NMR spectra of the dissolved perovskite solution were characterized on Bruker Avance III 400 MHz system. Thermogravimetric analysis (TGA) was measured on a Mettler-Toledo TGA/DSC1/1600HT. The elemental content in the perovskite thin films was evaluated by inductively coupled plasma mass spectrometry (ICP-MS, iCAP Q).

Synchrotron-based grazing incidence wide-angle x-ray scattering (GIWAXS) measurements were performed at the BL14B1 beamline of the Shanghai Synchrotron Radiation Facility (SSRF) using X-rays with a wavelength of 1.2398 Å. Two-dimensional (2D) GIWAXS patterns were acquired by a MarCCD detector mounted vertically at a distance of ~260 mm from the sample with a grazing incidence angle of 0.3°and an exposure time of 50 sec.

The in-situ GIWAXS measurements were performed at the BL14B1 beamline of the Shanghai Synchrotron Radiation Facility (SSRF) using a temperature dependent sample holder setup at X-ray wavelength of 0.6887 Å. Two-dimensional (2D) GIXRD patterns were acquired by a MarCCD mounted vertically at a distance ~466 mm from the sample with a grazing incidence angle of 0.20°and an exposure time of 30 sec.

The 2D GIWAXS patterns were analyzed using the FIT2D software and displayed in scattering vector q ($q = 4\pi\sin\theta/\lambda$) coordinates.

The *J-V* characteristics were measured with a Keithley 2401 source meter with a scan rate of 0.05 $V \cdot s^{-1}$ under the simulated AM 1.5G illumination (100 $mW \cdot cm^{-2}$) using Enlitech's 3A light source. The EQE was measured on a QE-3011 system (Enlitech). The size of the aperture for the J-V and EQE measurements is 3.5×3.5 and 10×10 mm^2, respectively.

The TPC/TPV (Zahner PP211 and Zahner Zennium) were generated by a microsecond pulse of a white light incident on solar cells under short circuit conditions (by a very low resistor

at 20 Ω) and open circuit condition (by a large resistor at 1 MΩ). No background light was applied.

Stability test

The test of the thermal stability of $CsPbI_3$ thin films was carried out with a 70 °C hotplate in a N_2 glove box. The photo-stability of the unencapsulated PSCs were tested by the following setup: a white LEDs lamp (100 $mW \cdot cm^{-2}$) continuously illuminated the PSC devices stored in a N_2 glove box at maximum power point (MPP). The photostability test for the encapsulation device in the ambient environment was carried out at MPP under the simulated AM 1.5G illumination (100 $mW \cdot cm^{-2}$) using Enlitech's 3A light source.

First-principles calculations.

Calculations of electronic band structures were performed within the framework of density functional theory (DFT) by using plane-wave pseudopotential methods as implemented in the Vienna Ab initio Simulation Package(*26, 27*). The electron−ion interactions were described by the projected augmented wave pseudopotentials (*28*) with the 5s, 5p and 6s (Cs), 5s, 5p (I) and 6s and 6p (Pb) electrons treated as valence electrons. The generalized gradient approximation formulated by Perdew, Burke, and Ernzerhof (*29*) was used as the exchange correlation functional. Kinetic Energy cutoff for the plane-wave basis set were set to 300 eV. The 5×5×5, 4×4×5 and 4×3×4 Γ-centered grids were used for electronic Brillouin zone integration for the α-phase, β-phase and γ-phase of $CsPbI_3$, respectively. The structures of all the phases were fully optimized with the residual forces on the atoms converged to below 0.01 eV/Å. To reduce the self-interaction error of DFT in band gaps calculations, we used the Heyd-Scuseria-Ernzerhof (HSE) hybrid functional approach with standard 25% exact Fock exchange (*30*). Spin–orbit coupling (SOC) is included.

Supplementary Text

β-$CsPbI_3$ formation

We first used TGA to explore the DMA volatilization from different sources. The TGA based thermogram suggests that DMAI can sublime at >250 °C from pure $DMAPbI_3$ powder, whereas the decomposition of $DMAPbI_3$ involving DMA liberation requires even higher temperatures (Fig.S3). Interestingly, the powder sample obtained by scratching the as-deposited precursor film of CsI+DMAI+PbI_2 shows decomposition features at <200 °C (Fig. S3).

Fig. S5 shows the UV-vis spectra and XRD patterns of the $CsPbI_3$ thin films using CsI+PbI_2·*x*DMAI (*x*=1.1-1.2) after different annealing stages. Initially, the peak corresponding to 11.8 degrees is assigned to $DMAPbI_3$. As annealing time increases, this peak disappears and $CsPbI_3$ perovskite forms. These results suggest that DMAI in PbI_2·*x*DMAI (*x*=1.1-1.2) should be an additive and helps control the crystallization of $CsPbI_3$ perovskite.

As the preparation of $CsPbI_3$ involves organic cation, we checked whether any DMA remains in $CsPbI_3$ using NMR and Tof-SIMS (Fig. S4 and S6). In Fig. S4, a strong NMR peak arising from the ammonium group of DMA appears in the as-spun perovskite films. However, during the annealing stage, the signals from $–NH_2^+–$ from DMA disappear (Fig. S4) confirming that DMAI works as a volatile additive for the controlling the growth of β-phase $CsPbI_3$ perovskite. Fig. S6 shows the absence of residual C from DMA in the $CsPbI_3$ perovskite. This is consistent with our XPS results for the $CsPbI_3$, where no N 1s signal was detected.

Compared to the standard XRD patterns of the different structures $CsPbI_3$ (*13*) with the previously reported α-$CsPbI_3$, we discovered that these $CsPbI_3$ with a bandgap of ~1.73 eV should be the γ-$CsPbI_3$. In present work, the as-achieved β-$CsPbI_3$ has a bandgap ~1.68 eV (Fig. S2). We further calculated the band gap of $CsPbI_3$ with different crystal phase, as shown in Fig. S10. Either

the band gaps based on the experimentally determined crystal structure or theoretically optimized crystal structure indicates that the β-$CsPbI_3$ with less distortion exhibited a lower band gap than the "γ-$CsPbI_3$". This result also confirmed that previously reported "α-$CsPbI_3$" with broader band gap than our β-$CsPbI_3$ should be "γ-$CsPbI_3$".

Energy level alignment of $CsPbI_3$ affected by CHI

The adsorption phenomena describing the interaction between β-$CsPbI_3$ and CHI layer are complex, and several factors may lead to the observed improved energy level alignment of the CHI-$CsPbI_3$ sample shown in Fig. 2D.

On the basis of our experimental results (e.g., UV-Vis, XRD, XPS, cross-sectional SEM), we propose that a thin-layer of CHI covers the β-$CsPbI_3$ film at its top and bottom interfaces as well as the grain-boundaries. The interaction between β-$CsPbI_3$ and the CHI layer are complex and several factors can contribute to the observed shifts in the energy levels of CHI-$CsPbI_3$ shown in the new Figure 2D. Thus, the positively charged ammonium groups of CHI may associate with negatively charged cesium vacancies at the $CsPbI_3$ surface becoming potential determining ions for the whole $CsPbI_3$ grain. This would explain the observed increase in the $CsPbI_3$ work function. The formation of interfacial dipoles between CHI and β-$CsPbI_3$ can induce similar shifts *(31-35)*.

From thermal admittance spectroscopy and density functional theory calculations, Zheng et al.(*20*) have previously reported that monolayers of these additives bind efficiently to both cationic (e.g., Pb cluster on MAI-terminated surface) and anionic (e.g., Pb-I antisites defects on the PbI_2-terminated surface) defects present at the $CH_3NH_3PbI_3$ perovskite surfaces. Considering that the probing depth of ultraviolet photoemission spectroscopy (UPS) is 2-3 nm, the UPS

spectra shown in Figure 2B represent in fact a convoluted signal from CHI and β-$CsPbI_3$ and interfaces between these two materials. Therefore, it is necessary to consider the UPS spectra of the CHI -covered $CsPbI_3$ grains as one system because of the strong interactions taking place at the interface and not as separated entities of CHI and β-$CsPbI_3$.

CHI treatment affected $CsPbI_3$ morphology

Based on the high-resolution SEM images for the $CsPbI_3$ (Fig. S15A and Fig. S20A) and CHI-$CsPbI_3$ (Fig. S15B and Fig. S20B) films, the $CsPbI_3$ film has some pinholes or cracks. However, the pinholes or cracks in the CHI-$CsPbI_3$ film (Fig. S15B) were filled with some fine grain after the CHI IPA post-treatment. ToF-SIMS was used to characterize the carbon element distribution in the cross-section of both $CsPbI_3$ and CHI-$CsPbI_3$ perovskite thin films (Fig. 2B-2C and Fig. S16). Fig. 2B indicates that no carbon element exists in the $CsPbI_3$ films. However, Fig. 2C and Fig. S16 reveals the existence of carbon element from CHI in the cross-section of the CHI-$CsPbI_3$ films. Both of these results confirm that CHI has filled into the bulk of the perovskite film through pinholes/cracks.

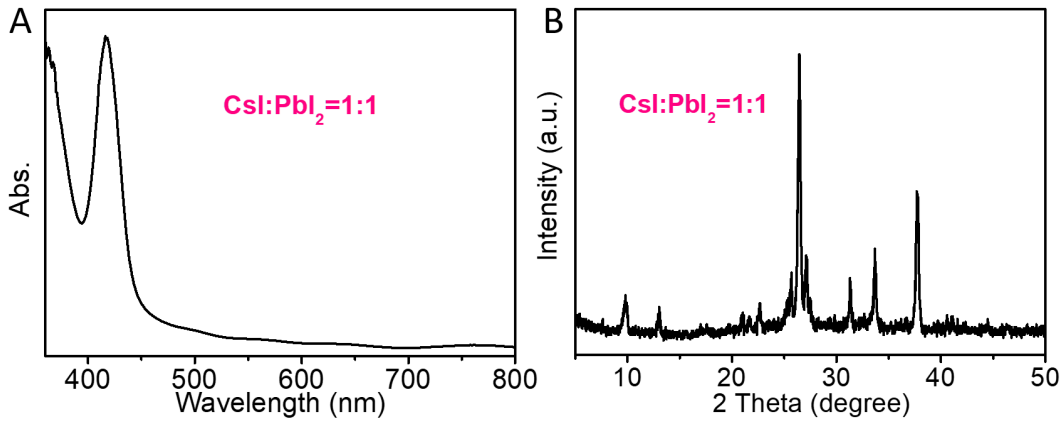

Fig. S1. (A) UV-vis spectrum and (B) XRD pattern of the $CsPbI_3$ thin films fabricated by $CsI+PbI_2$ with 210 °C-5min anneal.

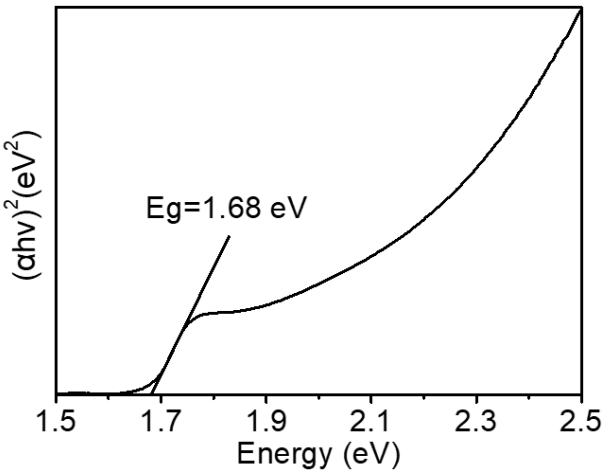

Fig. S2. Tauc plot of β-$CsPbI_3$ assuming direct band gap and showing determination of optical band gap from intercept.

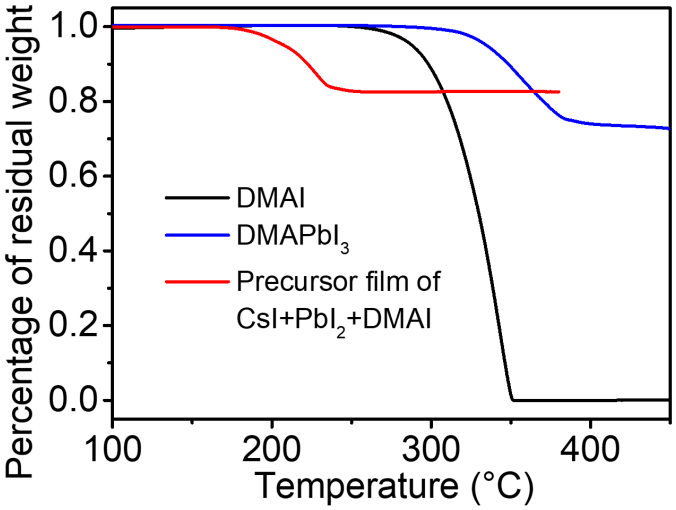

Fig. S3. Thermogravimetric analysis (TGA) of DMAI, $DMAPbI_3$ powders and powder scratched from the precursor film of $CsI+PbI_2+DMAI$.

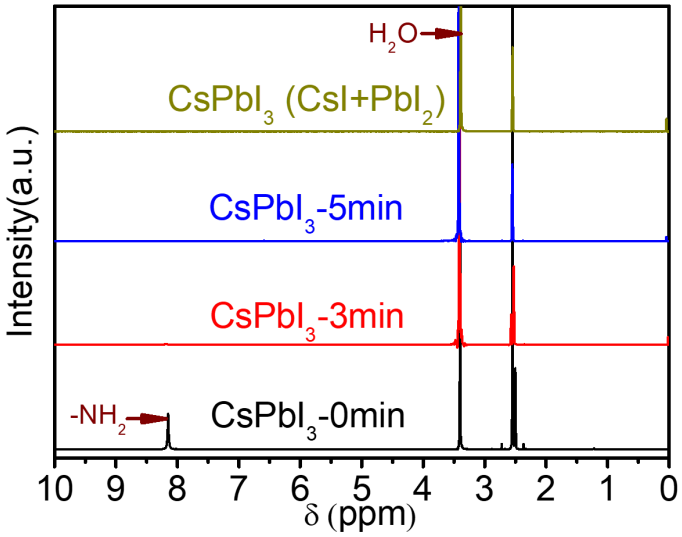

Fig. S4. 1H NMR of different annealing stages $CsPbI_3$ thin films (prepared by CsI + $PbI_2 \cdot x$DMAI) film and reference $CsPbI_3$ sample (prepared by CsI + PbI_2), which were dissolved in DMSO-d_6.

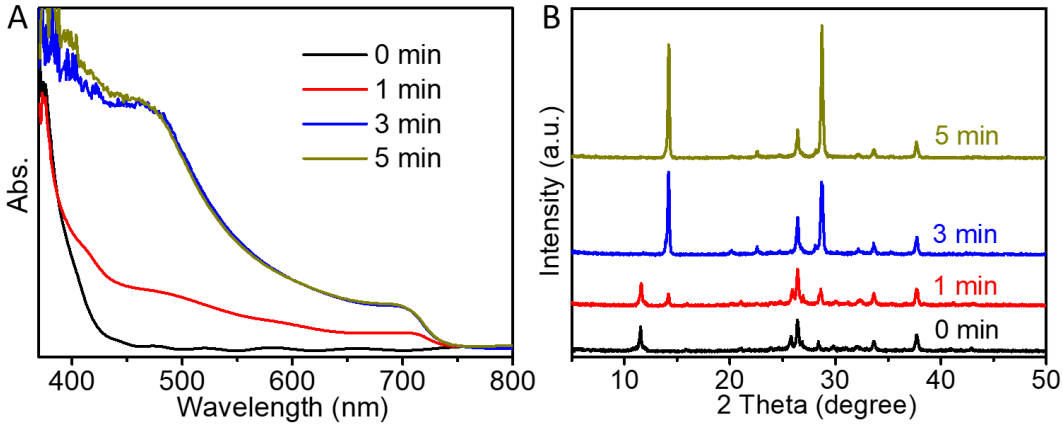

Fig. S5. (A) UV-vis spectra, (B) XRD patterns for $CsPbI_3$ thin films at different annealing stages.

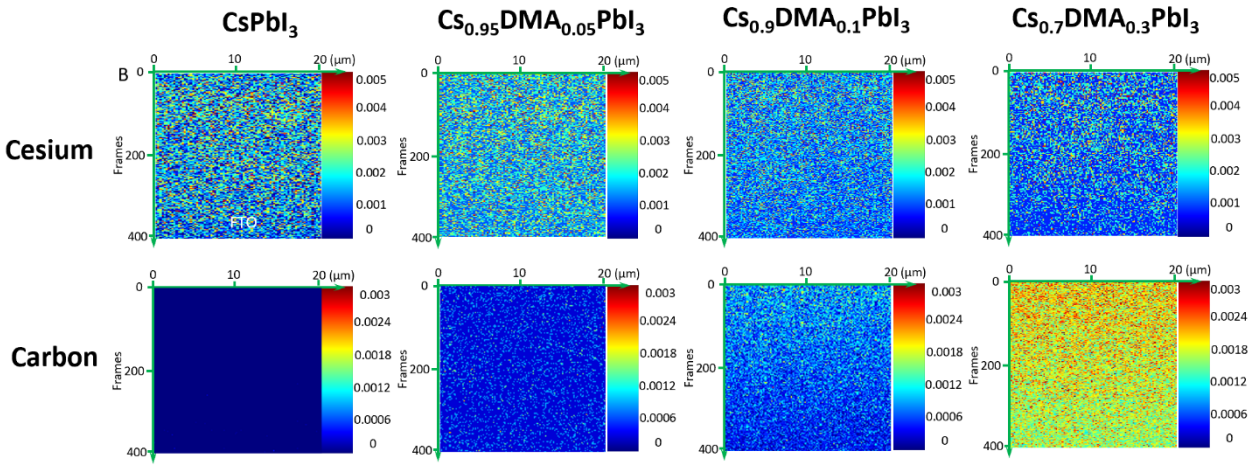

Fig. S6. Cross-sectional cesium and carbon elemental profile of $CsPbI_3$ and $Cs_{1-x}DMA\ xPbI_3$ (x=0.05, 0.1, 0.3) measured by TOF-SIMS:

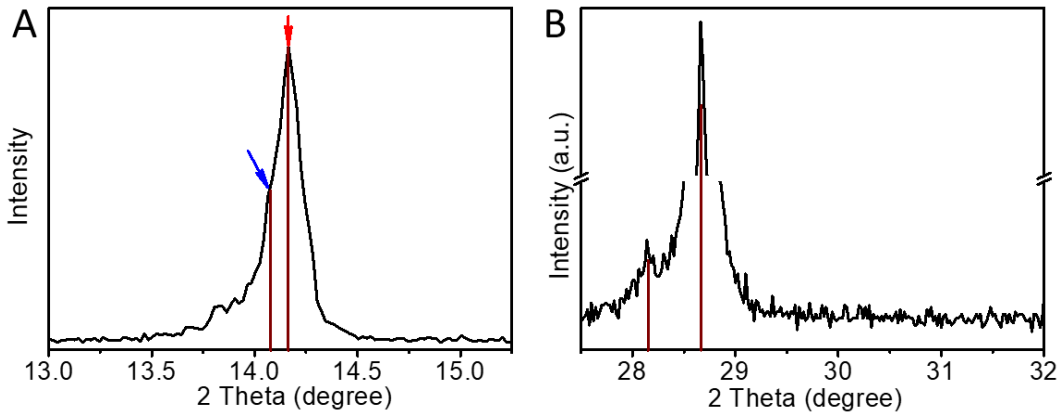

Fig. S7. Partially enlarged detail of the peak at (A) ~14° and (B) ~28°.

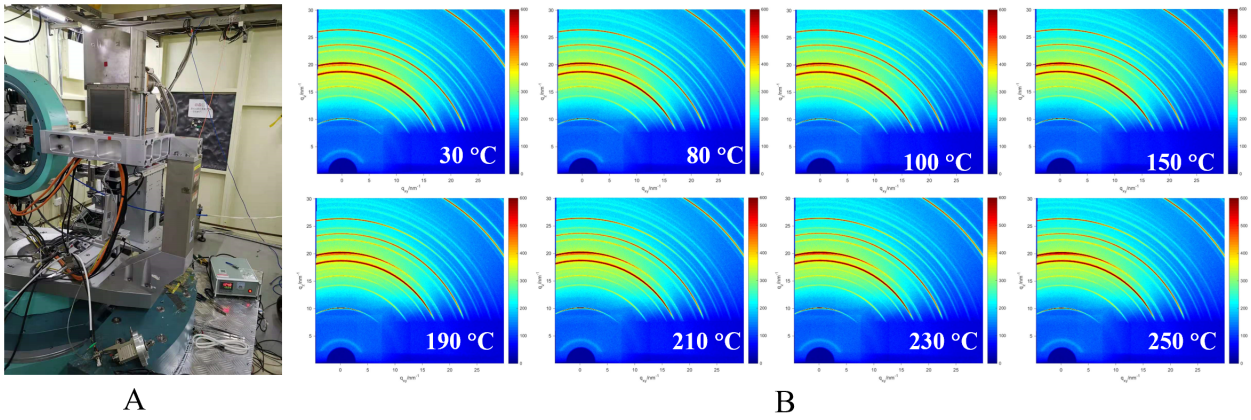

Figure S8. (A) A photograph of the experimental setup for the in-situ temperature dependent synchrotron-based GIWAXS measurements. (B) the two-dimensional (2D) GIWAXS patterns of the β-$CsPbI_3$ perovskite films annealing at different temperatures (30, 80, 100, 150, 190, 210, 230, 250 °C).

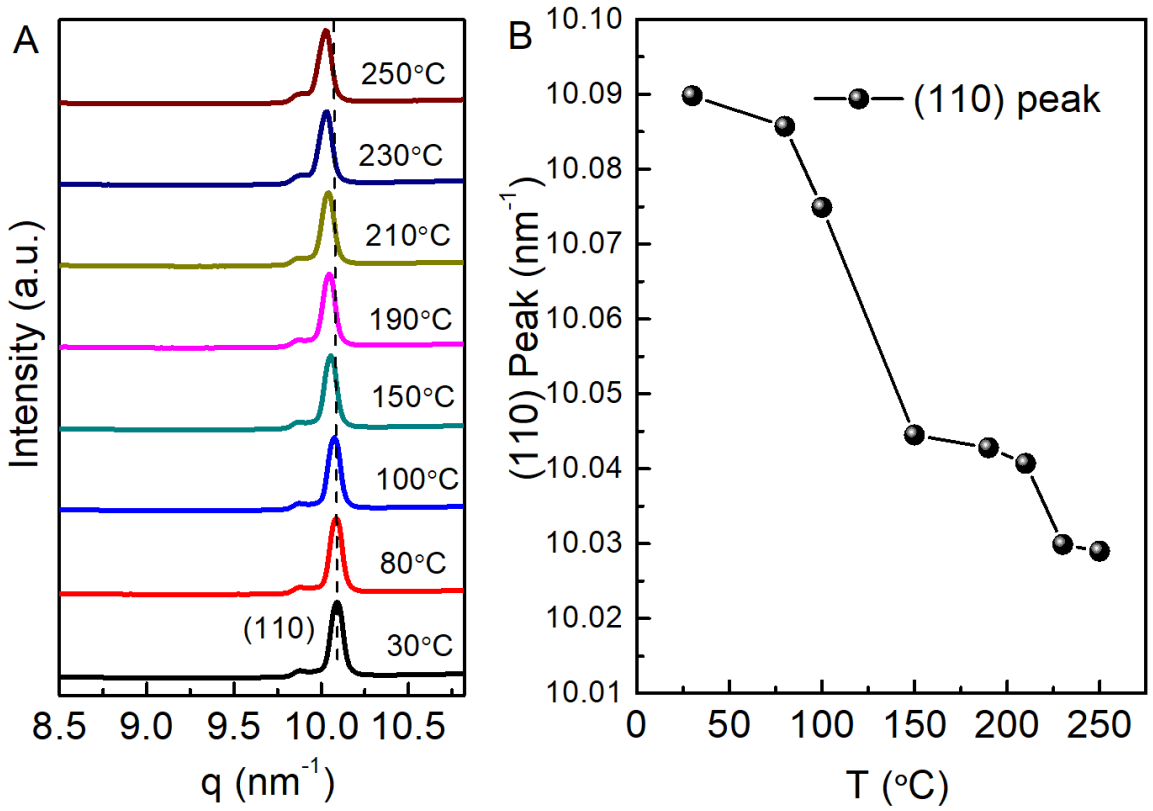

Figure S9. (A) The azimuthally integrated intensity profiles for the β-$CsPbI_3$ perovskite films annealing at different temperatures derived from Figure S8B. (B)The evolution of perovskite (110) peak positions obtained from the β-$CsPbI_3$ films as functions of the annealing temperature applied.

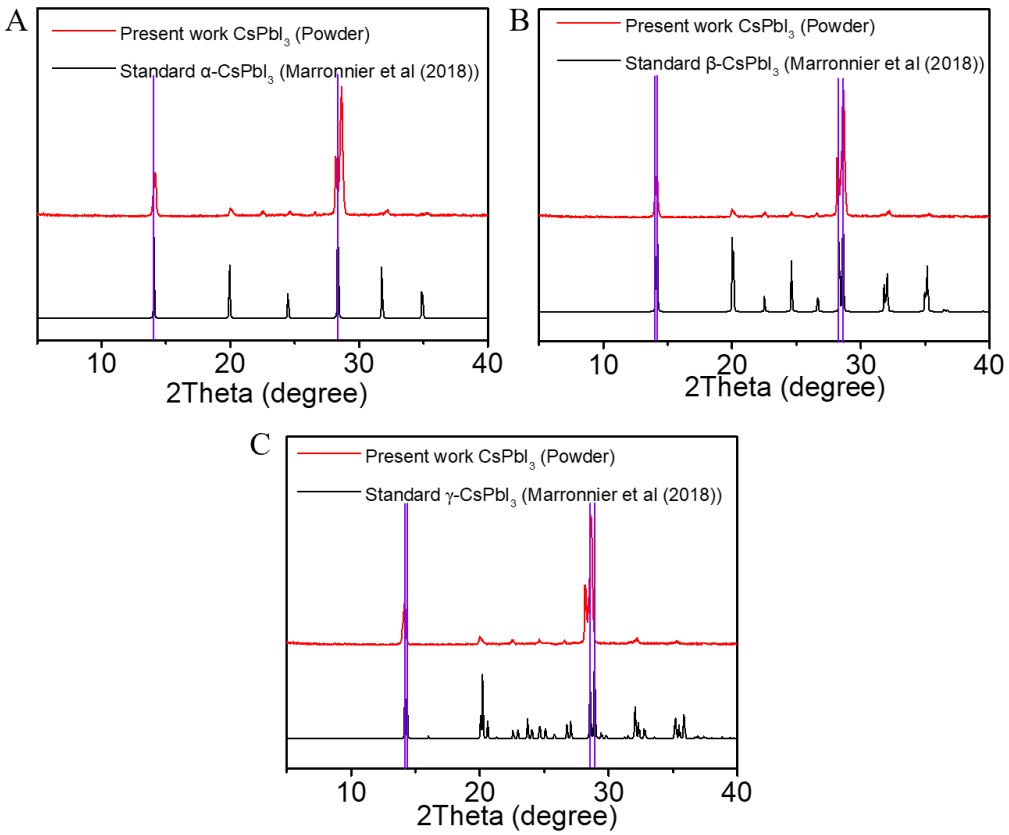

Fig. S10. Comparison of XRD patterns of β-$CsPbI_3$ powders scratched from a film with standard XRD patterns of (A) α-$CsPbI_3$, (B) β-$CsPbI_3$ and (C) γ-$CsPbI_3$.

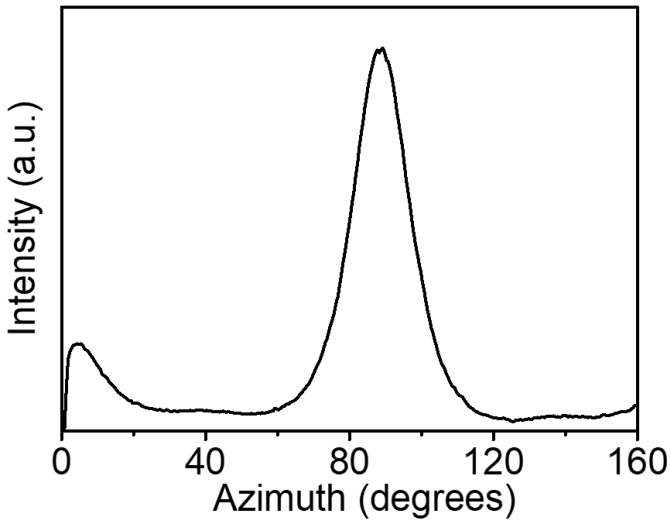

Fig. S11. Radially integrated intensity plots along the ring at q=10 nm^{-1} (scattering vector, $q=4\pi\sin(\theta)/\lambda$), which is assigned to the (110) plane of the $CsPbI_3$ thin film.

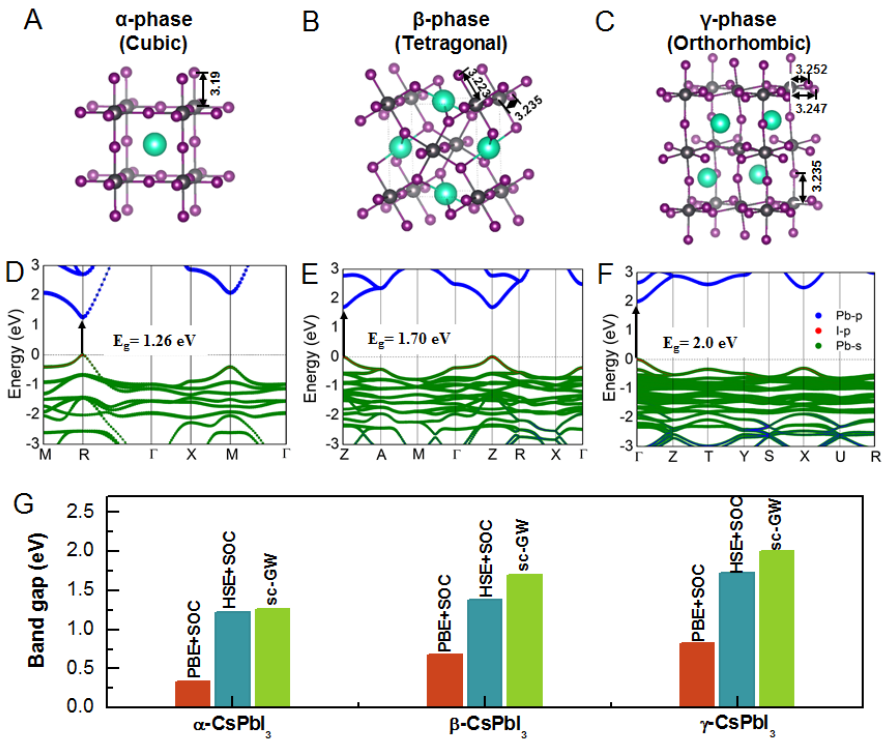

Fig. S12. The crystal structures (A-C) and band structures (D-F) of α-phase, β-phase and γ-phase $CsPbI_3$ perovskites. Theoretically optimized structural parameters were adopted. In (A-C) the explicit Pb-I bond lengths are indicated. In (D-F) the band structures are projected onto the composed atomic orbitals and the band gap values are corrected by the self-consistent GW approach, which minimizes the band gap underestimation issue of conventional DFT calculations. (G) summarizes the calculated band gaps of the three phases by using different approaches, i.e., the Perdew, Burke, and Ernzerhof exchange correlation functional with spin–orbit coupling included (PBE+SOC), the Heyd-Scuseria-Ernzerhof hybrid functional approach with SOC (HSE+SOC), and the self-consistent GW approach (sc-GW).

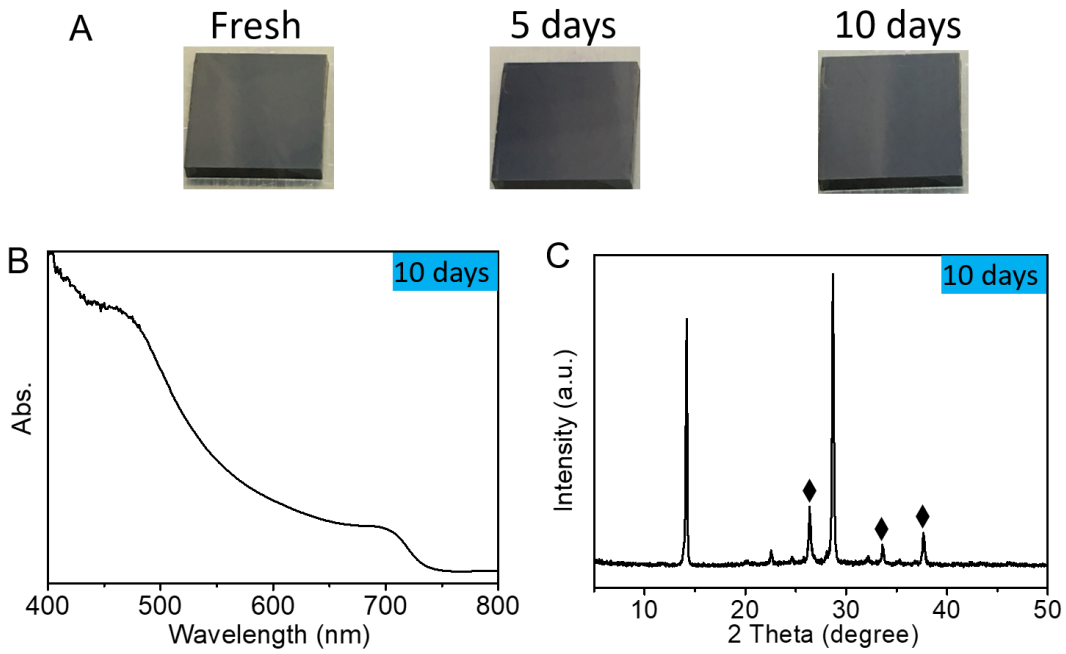

Fig. S13. Phase stability of the β-$CsPbI_3$ heated at 70 °C on a hotplate in N_2 glovebox. (A) Photographs and (B) UV-vis and (C) XRD evolution of the thin films 70 °C heated for 10 days, diamond symbols correspond to FTO substrate.

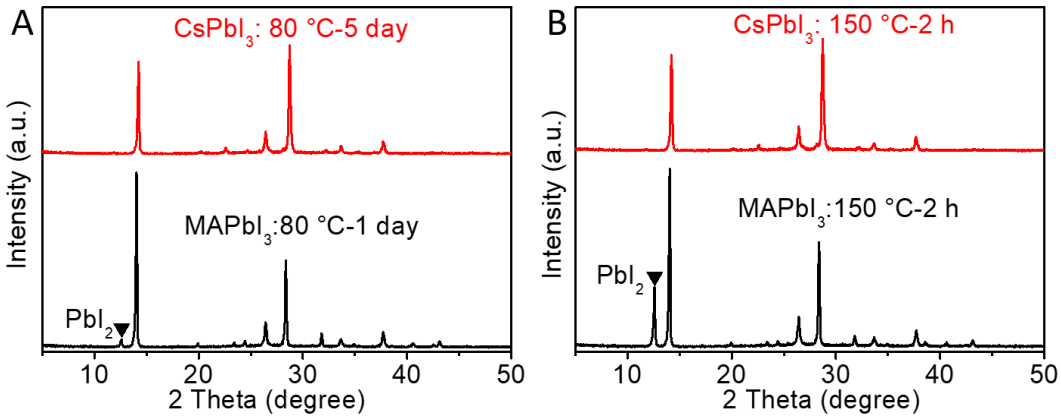

Fig. S14. Phase stability comparison for as-prepared $CsPbI_3$ and $MAPbI_3$ thin films at 80 °C and 150 °C, respectively**.**

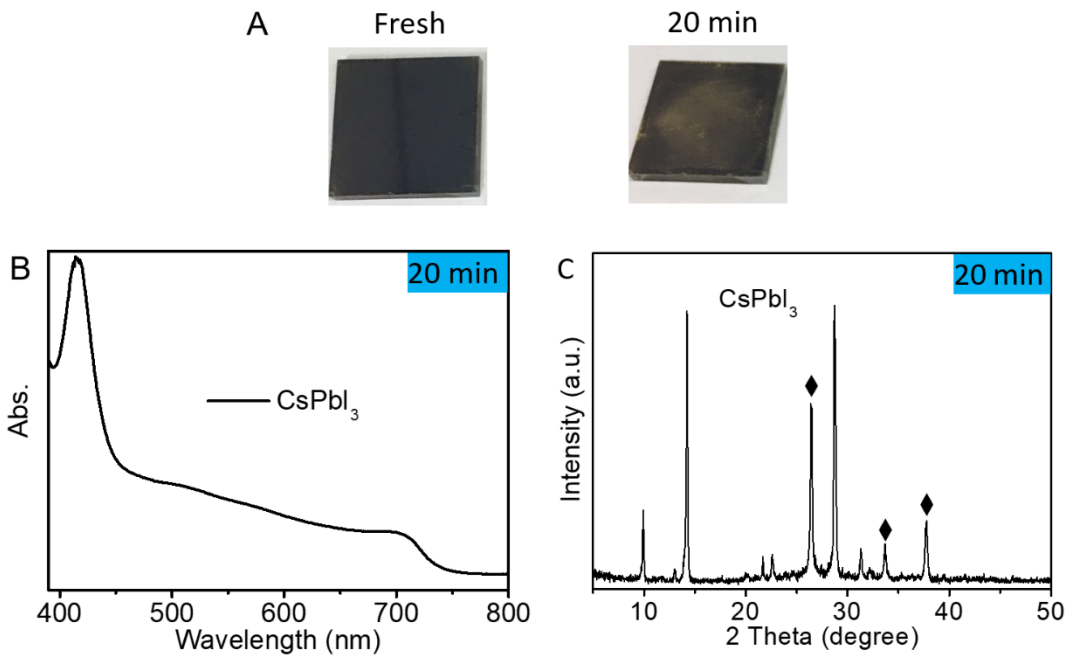

Fig. S15. Phase stability of the β-$CsPbI_3$ after exposed to an ambient environment with 85±5% RH at 30 °C for 20min. Corresponding (A) Photographs and (B) UV-vis and (C) XRD evolution of the thin films; diamond symbols correspond to XRD pattern of FTO substrate.

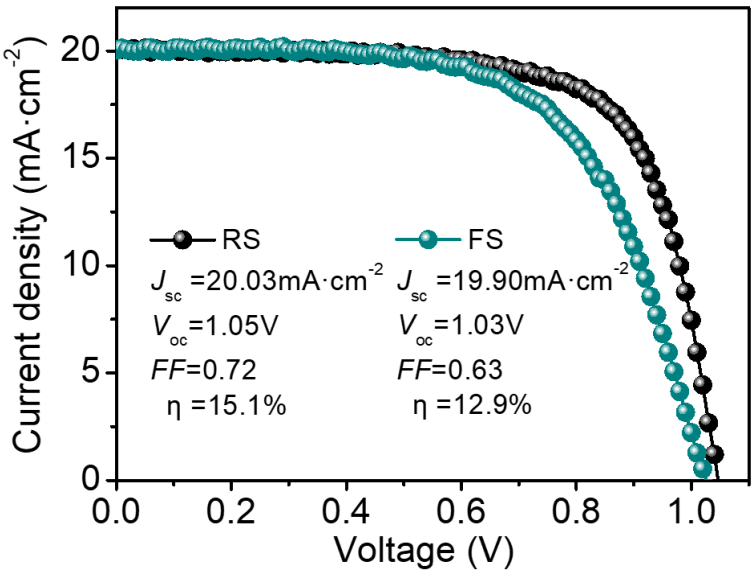

Fig. S16. J-V curves for PSCs based on β-$CsPbI_3$ in forward and reverse scans under simulated AM 1.5G solar illumination of 100 $mW \cdot cm^{-2}$.

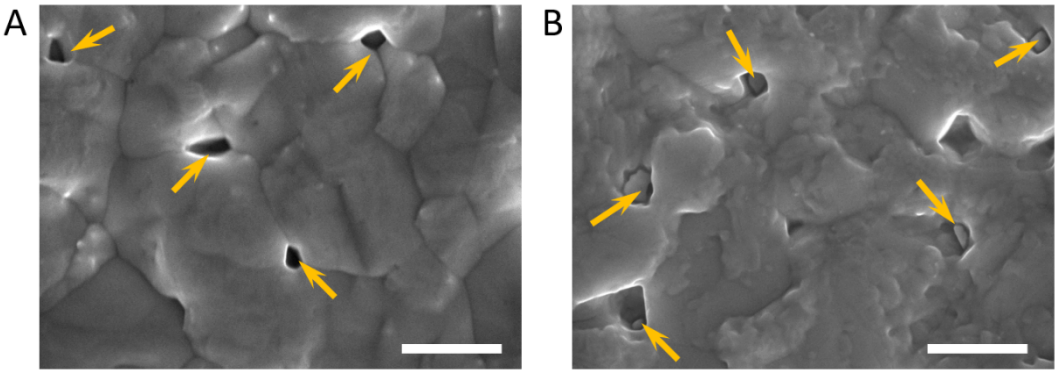

Fig. S17. High-magnification top-surface SEM image of (A) $CsPbI_3$ and (B) CHI-$CsPbI_3$ thin films, scale bars represent 500 nm.

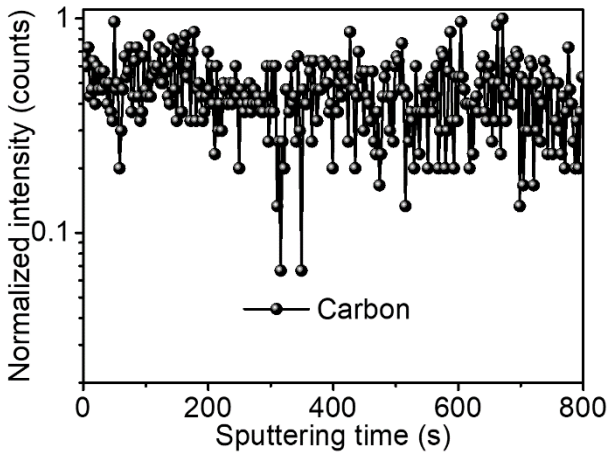

Fig. S18. ToF-SIMS cross-section profiles of the CHI-$CsPbI_3$ thin film showing the relative intensity for carbon across the film depth.

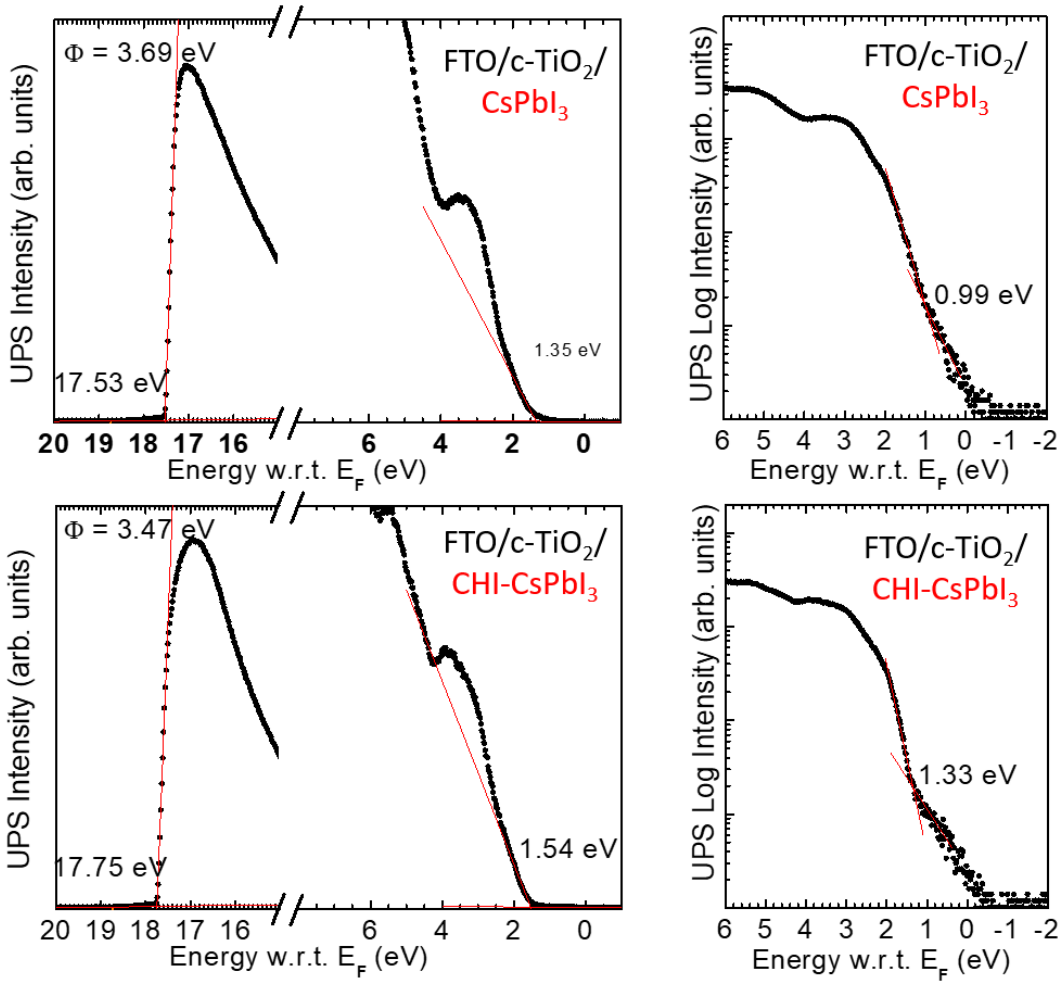

Fig. S19. UPS spectra (using He-I with photon energy of 21.22 eV) corresponding to the secondary electron onset region for the work function determination and the valence band region of the $CsPbI_3$, CHI-$CsPbI_3$ perovskite films deposited on FTO/c-TiO_2.

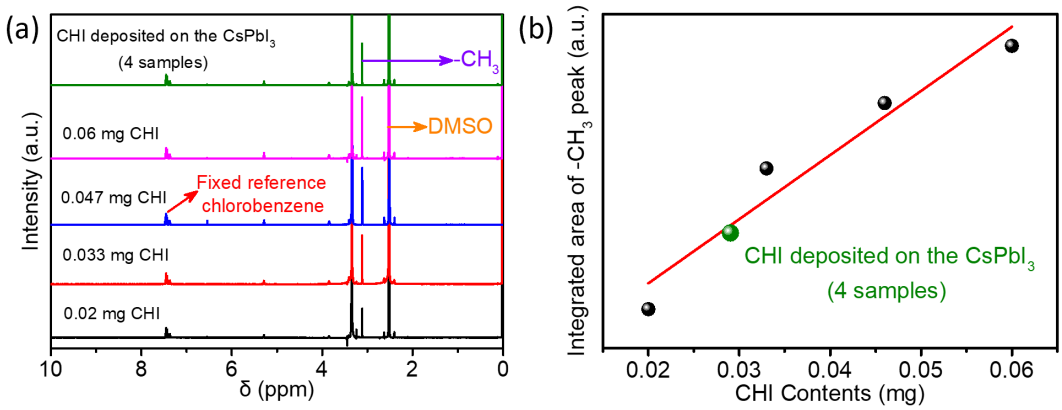

Fig. S20. (a). 1H NMR of different CHI contents and the CHI signal from 4 pieces of CHI-$CsPbI_3$ thin films, which were dissolved in DMSO-d6. The fixed chlorobenzene content was regarded as calibration reference. (b) Relationship between integrated area (-CH_3 peak from CHI) and CHI contents. The CHI contents of 4 pieces CHI-$CsPbI_3$ thin films is about ~0.029mg. Each CHI-$CsPbI_3$ thin films contains CHI about 0.00725 mg corresponding to ~1 weight % w.r.t. $CsPbI_3$.

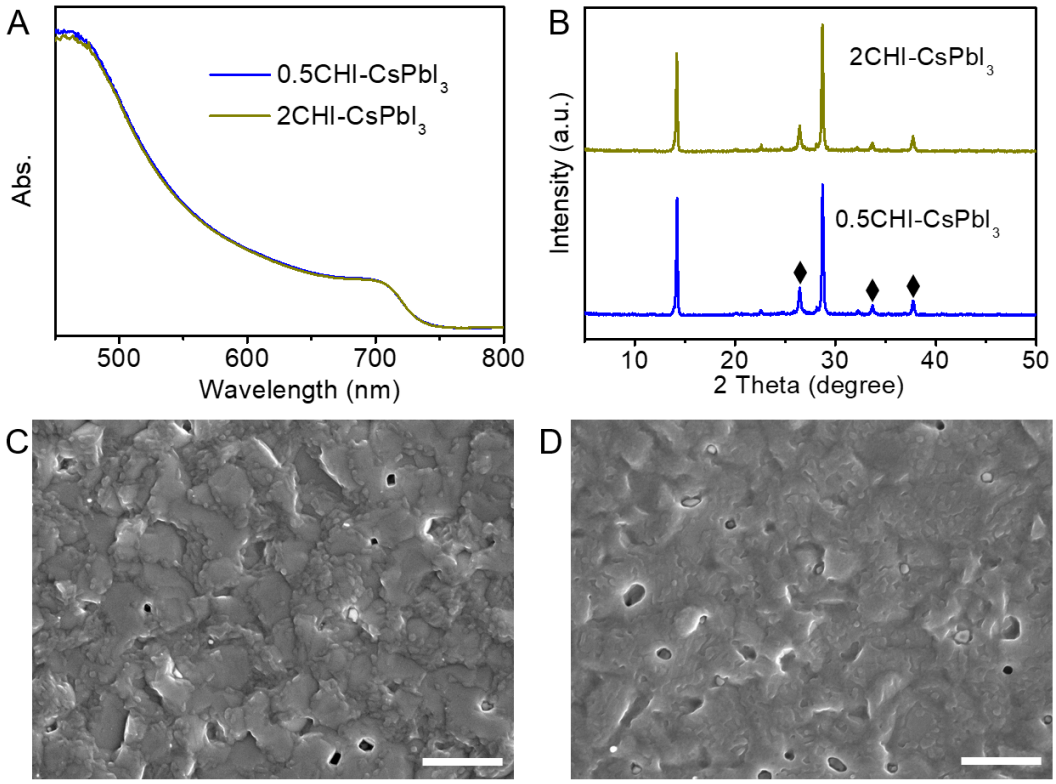

Fig. S21. CHI treatment effects on the spectroscopic and structural of β-$CsPbI_3$ perovskite thin films. (A) UV-vis and (B) XRD patterns of the 0.5 CHI-$CsPbI_3$ and 2 CHI-$CsPbI_3$ perovskite thin films. Diamond symbols correspond to FTO substrate. Top-surface SEM image of (C) 0.5 CHI-$CsPbI_3$ and (D) 2 CHI-$CsPbI_3$ perovskite thin films. Scale bars represent 1μm.

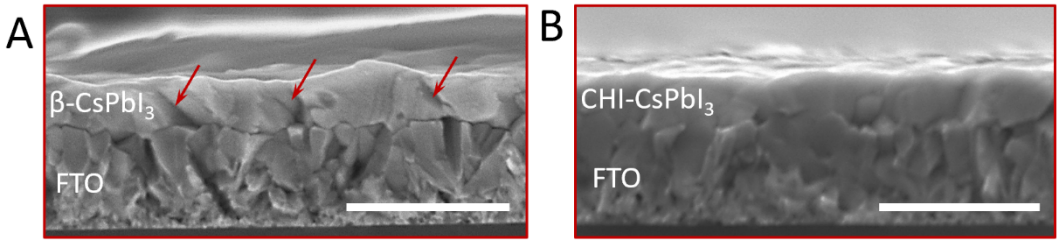

Fig. S22. SEM cross-sectional images of (A) the pristine β-$CsPbI_3$ sample and (B) the CHI-$CsPbI_3$ films, scale bars represent 1 μm.

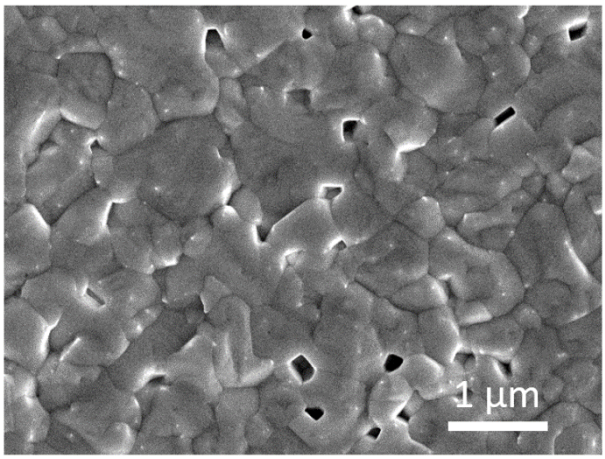

Fig. S23. Top-surface SEM image of $CsPbI_3$ perovskite films with only IPA treatment.

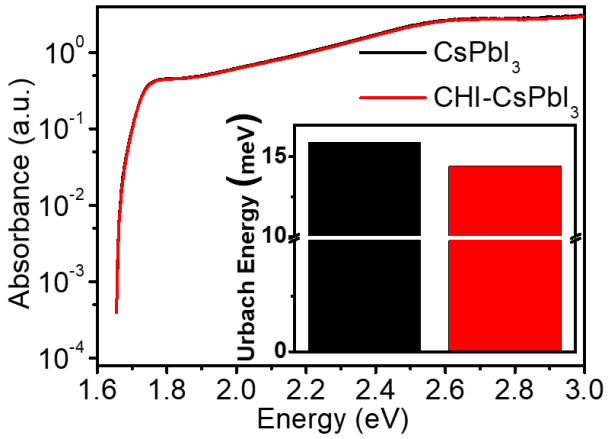

Fig. S24. Effective absorption coefficient of the $CsPbI_3$ and CHI-$CsPbI_3$ films. The inset shows the average Urbach energies for these samples.

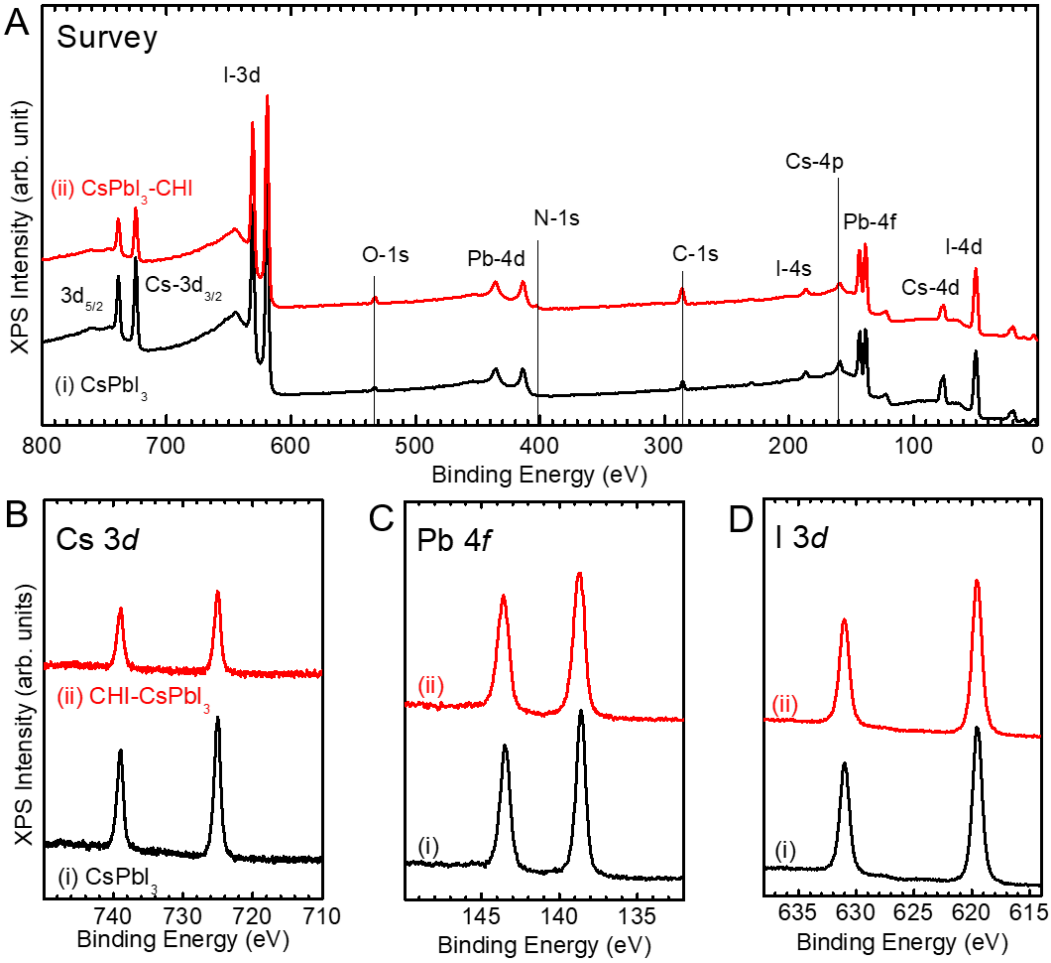

Fig. S25. (a) Survey XPS (using Al-K with photon energy of 1486.6 eV) and high resolution (b) Cs 3*d*, (c) Pb 4*f*, and (d) I 3*d* core-level spectra for the $CsPbI_3$ and CHI-$CsPbI_3$ perovskite films deposited on FTO/c-TiO_2.

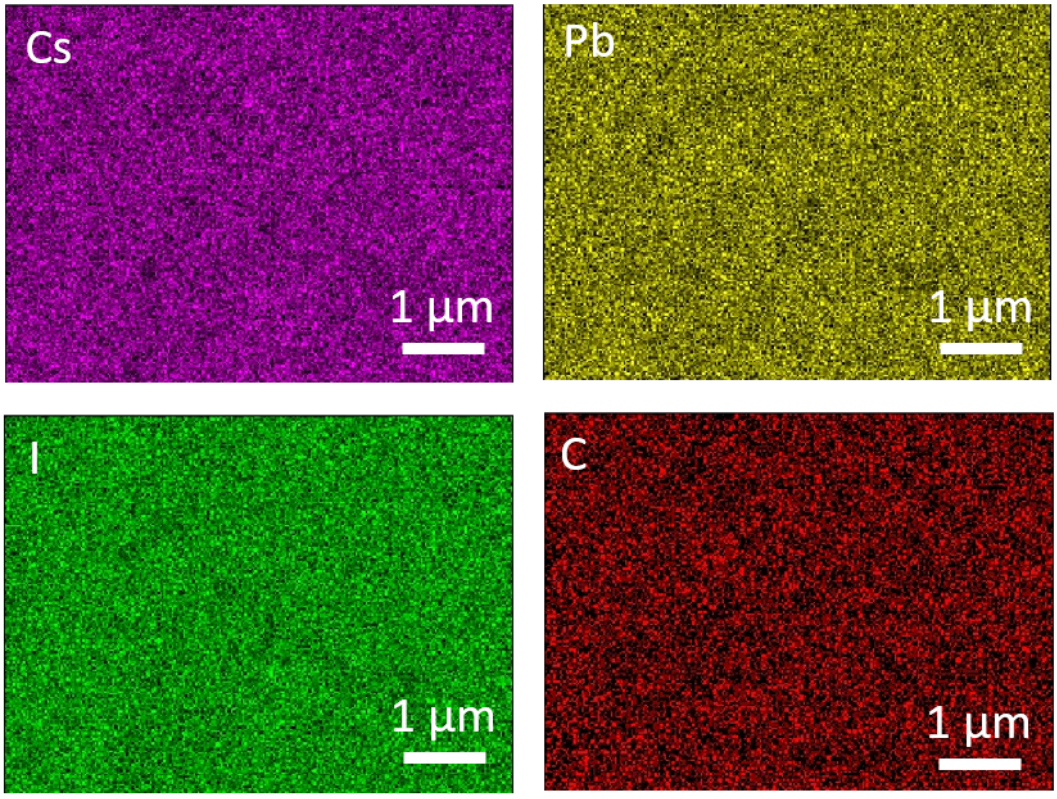

Fig. S26. EDX top view element mapping of the CHI-$CsPbI_3$ perovskite thin films.

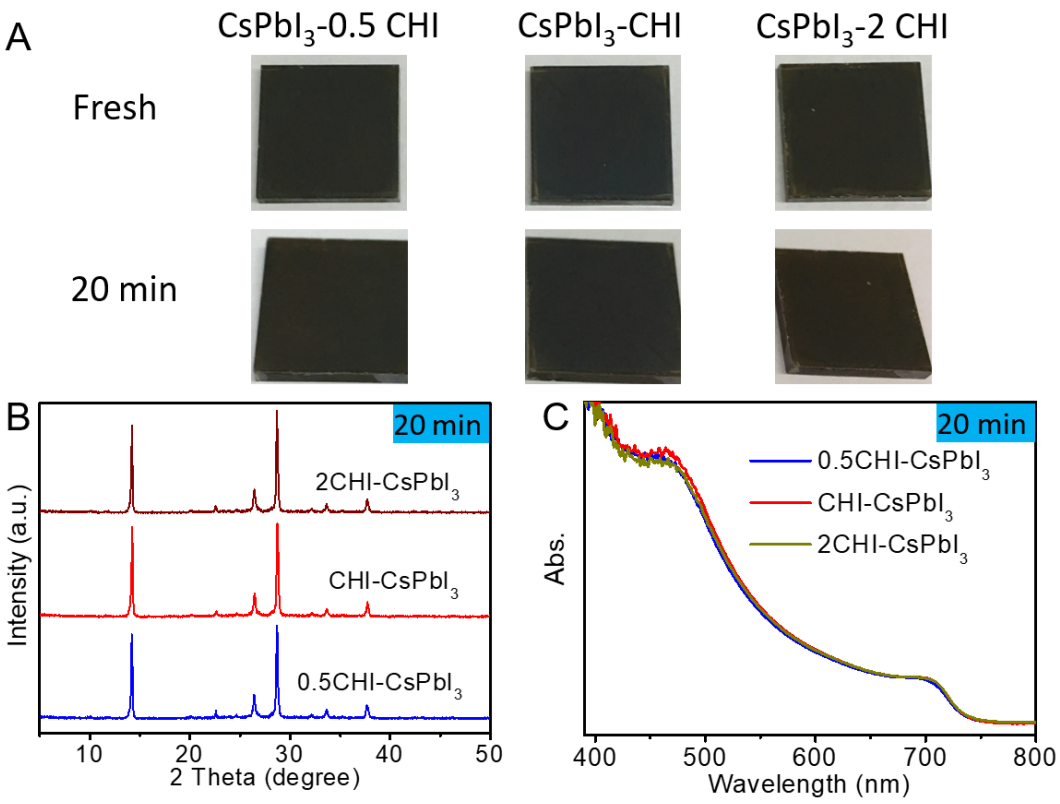

Fig. S27. Phase stability of the β-$CsPbI_3$ with CHI treatment after exposing to an ambient environment with 85±5% RH at 30 °C for 20min. Corresponding (a) photographs and (b) UV-vis and (c) XRD evolution of the thin films.

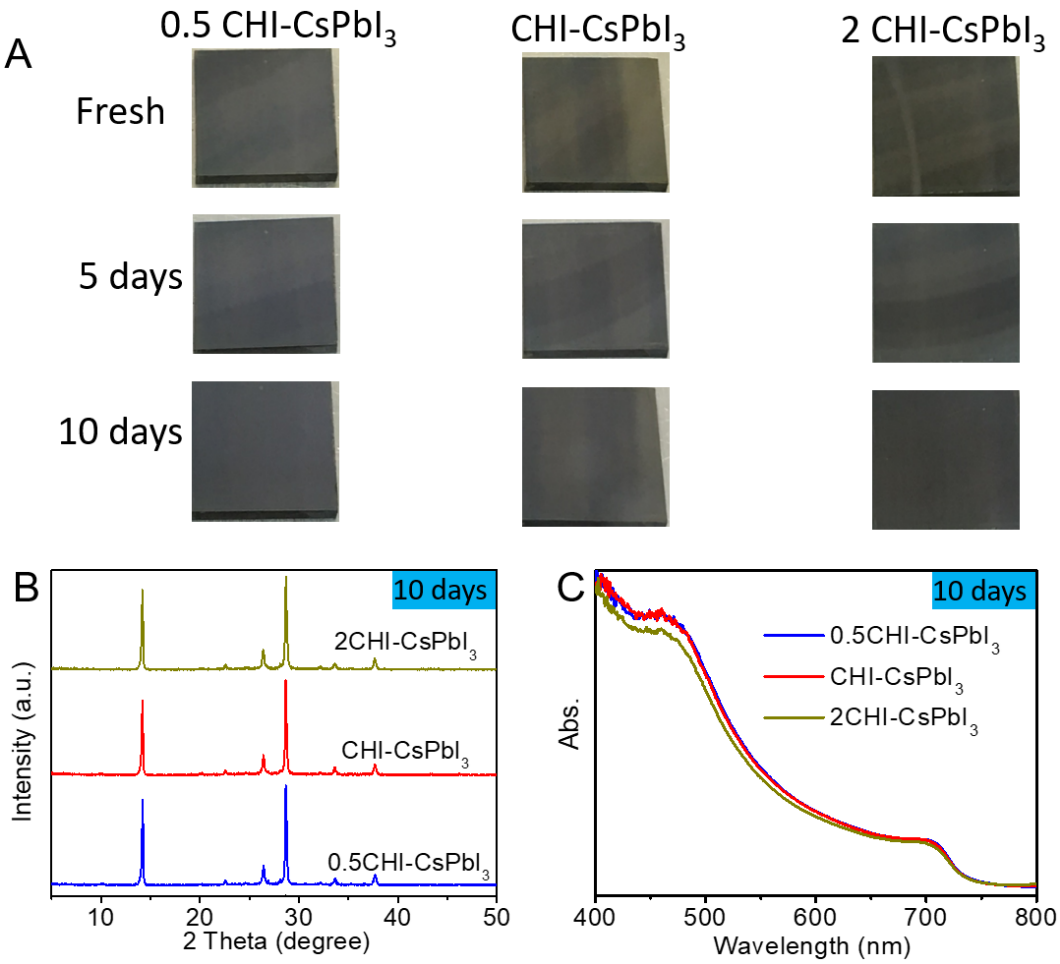

Fig. S28. Phase stability of the β-$CsPbI_3$ with CHI treatment heated on 70 °C hotplate in N_2 glovebox. (a) Photographs and (b) UV-vis and (c) XRD evolution of the thin films 70 °C heated for 10 days.

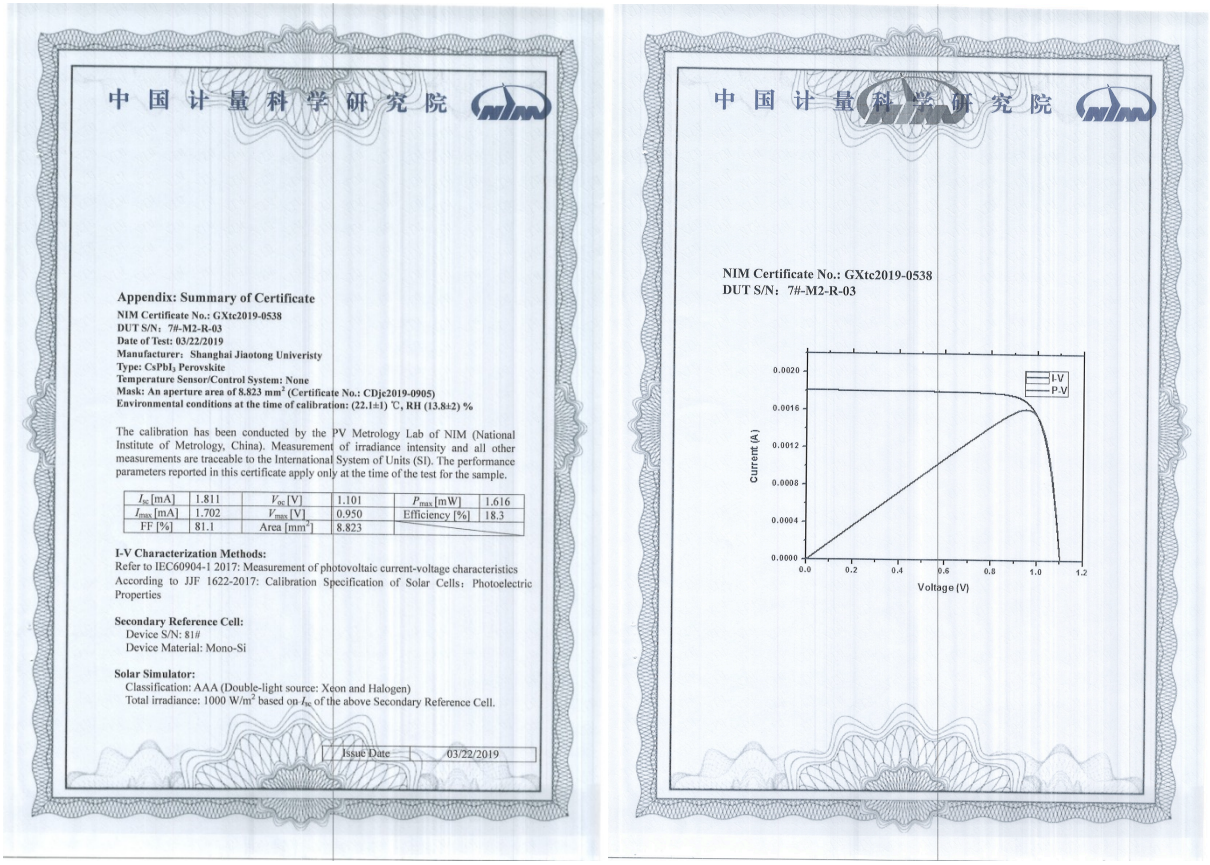

中 国 计 量 科 学 研 究 院

Appendix: Summary of Certificate

NIM Certificate No.: GXtc2019-0538
DUT S/N: 7#-M2-R-03
Date of Test: 03/22/2019
Manufacturer: Shanghai Jiaotong Univeristy
Type: $CsPbI_3$ Perovskite
Temperature Sensor/Control System: None
Mask: An aperture area of 8.823 mm^2 (Certificate No.: CDjc2019-0905)
Environmental conditions at the time of calibration: (22.1±1) ℃, RH (13.8±2) %

The calibration has been conducted by the PV Metrology Lab of NIM (National Institute of Metrology, China). Measurement of irradiance intensity and all other measurements are traceable to the International System of Units (SI). The performance parameters reported in this certificate apply only at the time of the test for the sample.

I_{sc} [mA]	1.811	V_{oc} [V]	1.101	P_{max} [mW]	1.616
I_{max} [mA]	1.702	V_{max} [V]	0.950	Efficiency [%]	18.3
FF [%]	81.1	Area [mm^2]	8.823		

I-V Characterization Methods:
Refer to IEC60904-1 2017: Measurement of photovoltaic current-voltage characteristics
According to JJF 1622-2017: Calibration Specification of Solar Cells: Photoelectric Properties

Secondary Reference Cell:
Device S/N: 81#
Device Material: Mono-Si

Solar Simulator:
Classification: AAA (Double-light source: Xeon and Halogen)
Total irradiance: 1000 W/m^2 based on I_{sc} of the above Secondary Reference Cell.

Issue Date	03/22/2019

中 国 计 量 科 学 研 究 院

NIM Certificate No.: GXtc2019-0538
DUT S/N: 7#-M2-R-03

Fig. S29. An independent PCE testing report of a CHI-$CsPbI_3$ based PSC device by an accredited PV Metrology Laboratory of NIM (National Institute of Metrology, China) verified a PCE of 18.30% (reverse scan, a *I*sc of 1.811 mA, a *V*oc of 1.101 V, and a FF of 81.1%). The cell was tested in air without encapsulation or protection during the testing process.

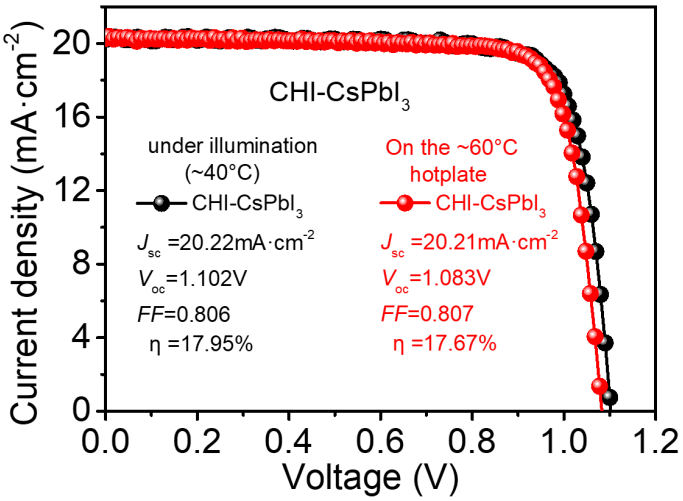

Figure S30. J-V characteristics of a typical CHI-$CsPbI_3$ PSC device measured under illumination (~40°C) and 60 °C hotplate.

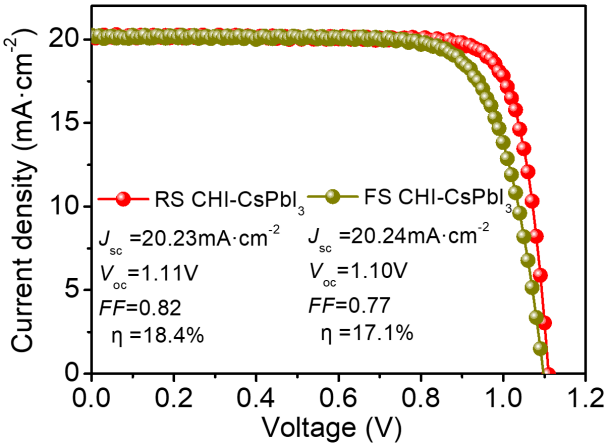

Fig. S31. *J-V* curves for PSCs based on CHI-$CsPbI_3$ in forward and reverse scans.

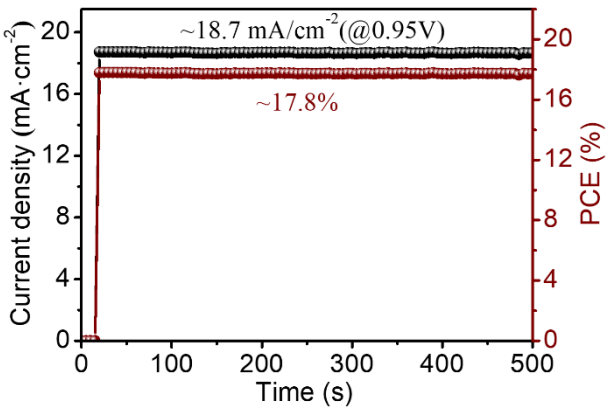

Fig. S32. PCE and *J* output at a maximum power point of 0.95 V for the CHI-$CsPbI_3$-based 'champion' PSC.

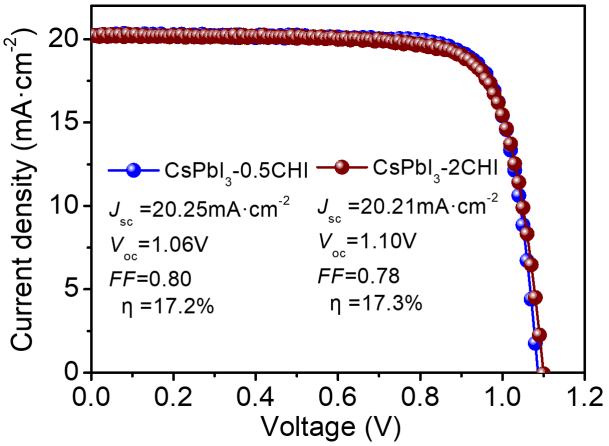

Fig. S33. *J-V* curves of PSCs based on $CsPbI_3$ (with different CHI treatment) in reverse scan.

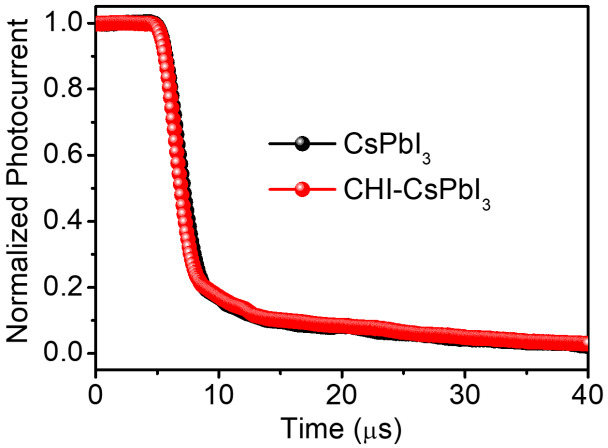

Fig. S34. TPC of $CsPbI_3$- and CHI-$CsPbI_3$- based devices.

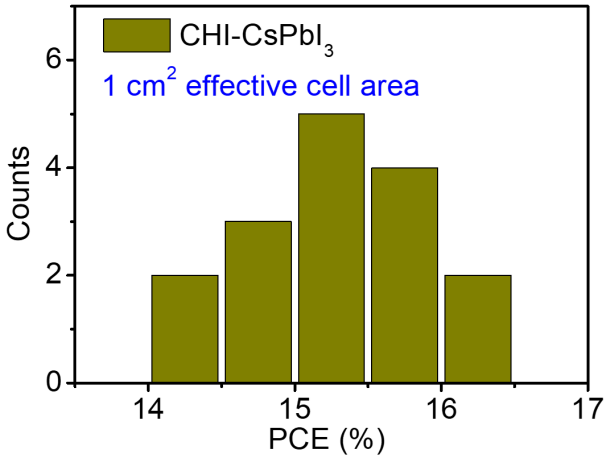

Fig. S35. PV performance statistics (1 cm^2 effective cell area; 16 devices) of PCSs based on CHI-$CsPbI_3$.

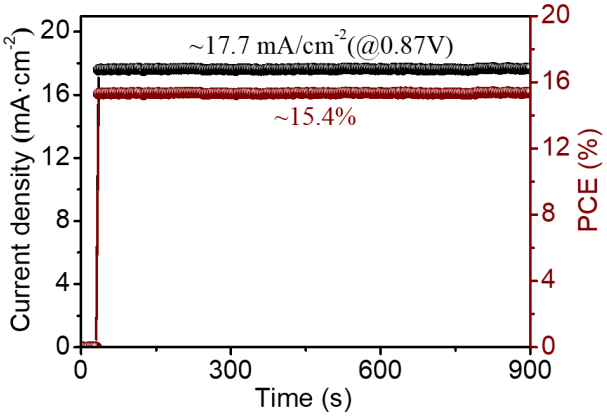

Fig. S36. PCE and *J* output at a maximum power point of 0.87 V for the large area CHI-$CsPbI_3$-based 'champion' PSC (1 cm^2 effective cell area).

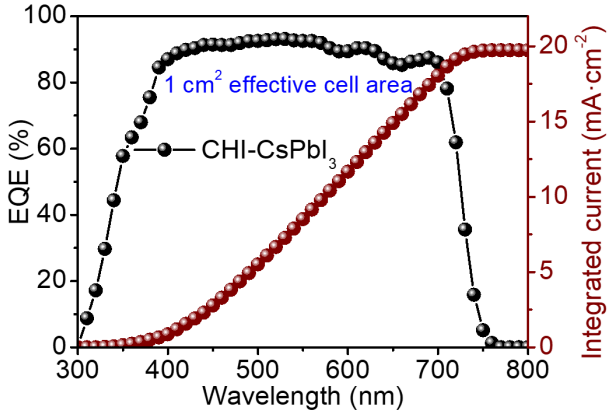

Fig. S37. EQE spectrum together with the integrated J_{SC} for the large area CHI-$CsPbI_3$ based PSCs.

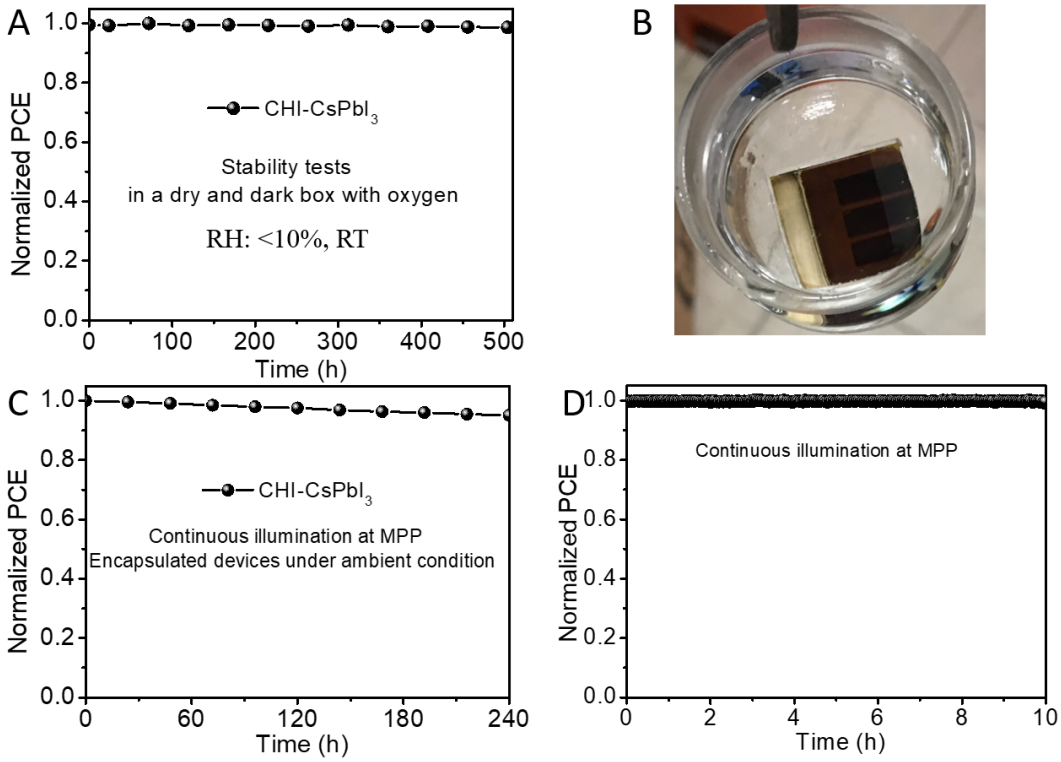

Fig. S38. (A) PCE of the PSC based on CHI-$CsPbI_3$ as a function of storage time in a dark and dry box at <10% RH and room temperature; (B) Photograph of the encapsulated CHI-$CsPbI_3$ PSC device placed in water, (C) Photostability of the encapsulated CHI-$CsPbI_3$ PSC devices in air under the simulated AM 1.5G illumination (100 $mW \cdot cm^{-2}$) using Enlitech's 3A light source at their MPP. (D) A typical stable output of 10h MPP measurement in Fig. S38C.

Table S1 Element contents in $CsPbI_3$ and $Cs_{0.7}DMA_{0.3}PbI_3$ powders measured by ICP-MS method.

	Cs (ppm)	Pb (ppm)	Cs: Pb molar ratio
$CsPbI_3$	17944.8532	27829.9315	1.003
$Cs_{0.7}DMA_{0.3}PbI_3$	10190.4395	22764.4856	0.697

Table S2 Average PV parameters of large-area PSCs based on CHI-$CsPbI_3$ (1 cm^2 effective cell area; 16 devices)

	J_{sc}/mA·cm^{-2}	V_{oc}/V	*FF*	PCE/%
$CsPbI_3$-CHI	19.41±0.17	1.095±0.018	0.716±0.018	15.2±0.6